Turbulent structures in cylindrical density currents in a rotating frame of reference

Jorge S. Salinas[a], Mariano I. Cantero[a,b], Enzo A. Dari[a,b] and Thomas Bonometti[c]

[a]Comisión Nacional de Energía Atómica e Instituto Balseiro, Centro Atómico Bariloche, San Carlos de Bariloche, Argentina; [b]Consejo Nacional de Investigaciones Científicas y Técnicas, San Carlos de Bariloche, Argentina; [c]Institut de Mécanique des Fluides de Toulouse (IMFT) – Université de Toulouse, CNRS-INPT-UPS, Toulouse, France

ABSTRACT

Gravity currents are flows generated by the action of gravity on fluids with different densities. In some geophysical applications, modeling such flows makes it necessary to account for rotating effects, modifying the dynamics of the flow. While previous works on rotating stratified flows focused on currents of large Coriolis number, the present work focuses on flows with small Coriolis numbers (i.e. moderate-to-large Rossby numbers). In this work, cylindrical rotating gravity currents are investigated by means of highly resolved simulations. A brief analysis of the mean flow evolution to the final state is presented to provide a complete picture of the flow dynamics. The numerical results, showing the well-known oscillatory behavior of the flow (inertial waves) and a final state lens shape (geostrophic adjustment), are in good agreement with experimental observations and theoretical models. The turbulent structures in the flow are visualized and described using, among others, a stereoscopic visualization and videos as supplementary material. In particular, the structure of the lobes and clefts at the front of the current is presented in association to local turbulent structures. In rotating gravity currents, the vortices observed at the lobes front are not of hairpin type but are rather of Kelvin-Helmholtz type.

KEYWORDS

Gravity currents; rotation effects; turbulent flows; direct numerical simulation

1. Introduction

Gravity or density currents are flows generated by the action of gravity on fluids with different density. These flows manifest as currents of light fluid above a heavy fluid or as currents of heavy fluid below light fluid. Gravity currents are important flows in many engineering and geophysical problems. Gravity currents are known to move and transport large amounts of mass and energy [1]. Some examples of these flows are snow avalanches in the mountains, volcanic plumes, sand storms turbidity currents in the desert and oils spills [1–3].

Rotational effects on gravity currents completely change the dynamics of the flow by hindering free spreading [4,5]. In the turbulent regime, gravity currents are of a non-linear

CONTACT Jorge S. Salinas josalinas@ufl.edu

nature and exhibit a wide range of temporal and spatial scales [6]. Rotational effects bring in another level of complexity to these flows, which make detailed modelling a difficult task.

When gravity currents are restricted laterally, they spread with a statistically planar front [7]. On the other hand, when the currents spread out in an horizontal plane with unhindered motion in all directions, the front acquires a nominal cylindrical shape (see e.g. experimental pictures in [8]). Non-rotating planar and cylindrical gravity currents have been extensively studied analytically, experimentally and numerically. References [9] and [7] are pioneering works that have addressed the lobe and cleft structure at the front of planar gravity currents. Great effort has been devoted to understand and explain the different phases of spreading of gravity currents (see e.g. [10–13]). Patterson et al. [14] and Alahyari and Longmire [15] have studied the internal structure of gravity fronts (see also [16–19]). Three-dimensional highly resolved simulations of planar gravity currents have been performed by Hartel et al. [20], Blanchette et al. [21], Birman et al. [22] and Cantero et al. [6,23]. Three-dimensional highly resolved simulations of non-rotating cylindrical density currents have been performed by Cantero et al. [8].

The rotation of the system imposes an intrinsic time scale $T_C = 1/\Omega_z$ at which rotational effects will impact the flow, where Ω_z is the angular velocity of the rotating system in the direction normal to the flow spreading direction. On the other hand, gravity current fronts develop with a characteristic time scale $T = r_0/U$, where U is the characteristic velocity of the gravity current front and r_0 is the characteristic length scale for the front spreading (see Section 2 for precise definitions). The ratio of these two time scales is the Coriolis number $\mathcal{C} = T/T_C$ (or equivalently the Rossby number $Ro = T_C/T$).

Gravity currents subject to rotation have been studied by a number of authors. Hallworth et al. [24] report experimental and numerical investigations of cylindrical gravity currents in a rotating system with focus on the front dynamics in the range $0 \leq \mathcal{C} \leq 0.4$. Stegner et al. [25,26] addressed the geostrophic adjustment of cylindrical fronts experimentally in the range $0.4 \leq \mathcal{C} \leq 1.8$ (see also [27]). The book by Ungarish [28] presents great detail of analytic models for rotating gravity currents (see also [29,30]). Recently, Salinas [31] has performed highly resolved simulations of Coriolis effects on planar and cylindrical gravity currents. As pointed out by Griffiths [4], 'the vast body of work on instability in rotating stratified fluids has assumed small Rossby numbers and small variations of layer depth, and therefore does not capture the physics of density fronts' (see e.g. [5,25,32–34]). The present work focuses on flows with small Coriolis numbers (equivalently large Rossby numbers) for which $T < T_C$. Thus, the gravity current flows addressed in this work develop first their intrinsic characteristics which are later affected by rotational forces.

Rotating cylindrical gravity currents are investigated by means of highly resolved numerical simulations. Six three-dimensional simulations are reported with grid resolutions up to 165-million points [31], various boundary conditions ('free-slip' and 'no-slip'), two Reynolds numbers and three Coriolis numbers. The work mainly focuses on describing the turbulent structures present in the flow and their dynamics. We also report on the formation and evolution of the lobe and cleft structure at the front. Although the adjustment to the geostrophy is a well-known process (see e.g. [32]), a brief analysis and description of the mean flow evolution to the final state is presented to provide a complete picture of the flow dynamics and to stress the effect of friction at the bottom. Results such as the maximum distance of propagation of the front in the first oscillation, the frequency of the successive outward fronts oscillation and the final lens shape of the current are reported

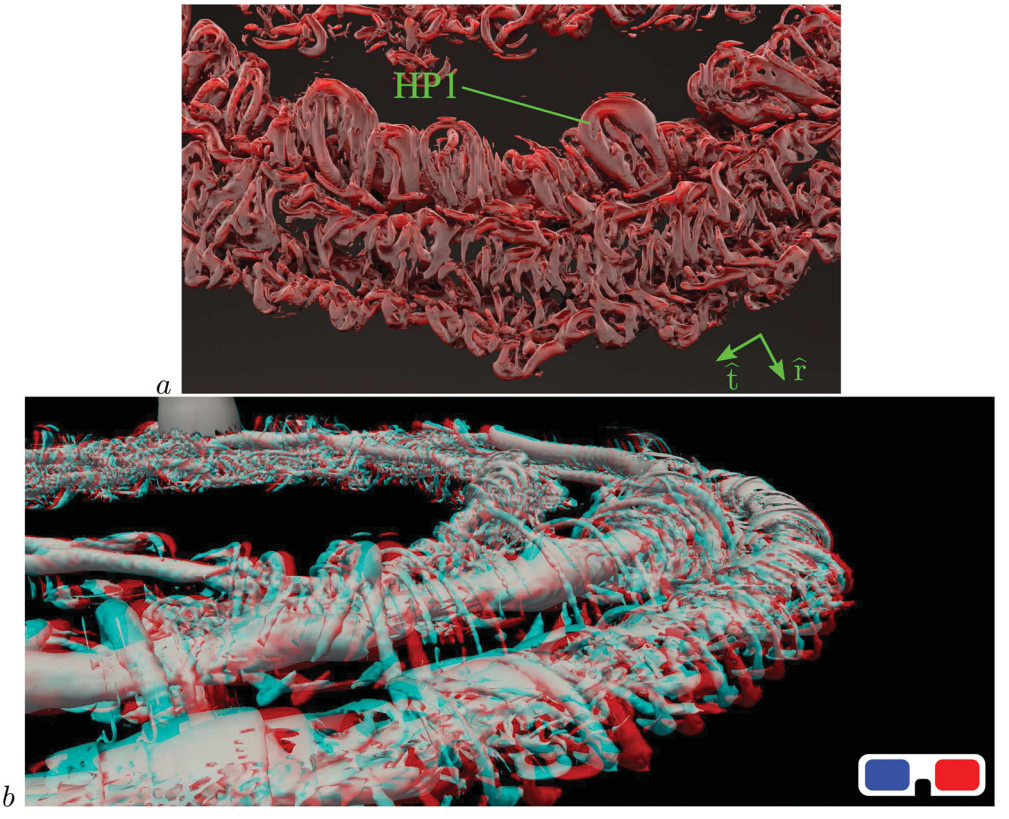

Figure 1. (a) Closeup bottom view of the hairpin vortices *HP*1 for case (5) at $\tilde{t} = 6.25$ visualised by an iso-surface of $\tilde{\lambda}_{ci} = 3$. Also depicted are the radial ($\hat{\mathbf{r}}$) and tangential ($\hat{\mathbf{t}}$) axis. (b) Stereoscopic visualisation of vortex structures for case (5) at $\tilde{t} = 5$ visualised by the iso-surface of swirling strength $\tilde{\lambda}_{ci} = 2$. The figure must be viewed with red–blue glasses.

and compared to theoretical models and available laboratory observations. Supplementary material videos are available and referenced throughout the work.

2. Mathematical and numerical formulation

The problem under consideration is depicted schematically in Figure 2. It consists of a rectangular tank rotating counterclockwise at a constant angular velocity Ω_z along the vertical axis z.

Co-rotating with the tank is heavy fluid of density ρ_1, initially confined in a cylindrical region of radius r_0, occupying the full height of the domain H (blue shaded area in Figure 2), and initially separated by a vertical partition from the lighter ambient co-rotating fluid of density ρ_0 (not shown). The heavy fluid is then released (at time zero) and the flow spreads in the horizontal direction (x and y). A schematic representation of the density current spreading is presented in Figure 2 as a gray shaded region.

This work considers flows in which the density difference between the heavy fluid and lighter ambient fluid is small enough that the Boussinesq approximation is valid. Under

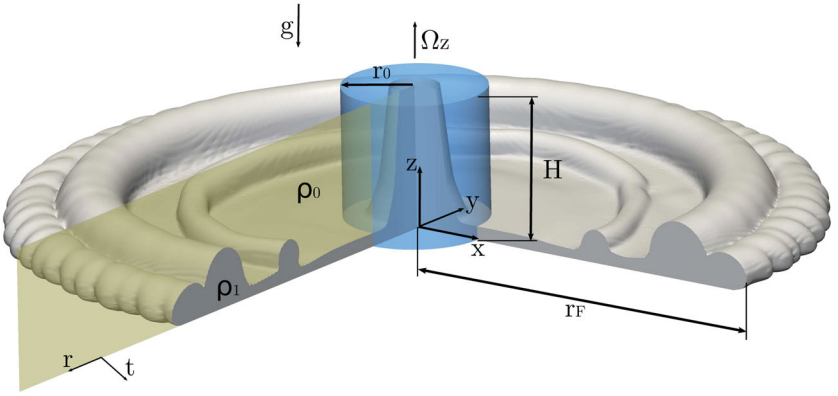

Figure 2. Schematic of the configuration for the cylindrical system. The system is rotating at a constant angular velocity Ω_z along the vertical axis z counterclockwise. Also depicted are the axis used to compute the mean flow (radial $\hat{\mathbf{r}}$ and tangential $\hat{\mathbf{t}}$ axis).

these circumstances, and in a reference frame attached to the rotating tank, the dimensionless governing equations are [24,28]

$$\frac{\partial \tilde{\mathbf{u}}}{\partial \tilde{t}} + \tilde{\mathbf{u}} \cdot \tilde{\nabla} \tilde{\mathbf{u}} = -\tilde{\nabla} \tilde{p} + \frac{H}{r_0} \frac{1}{\mathrm{Re}} \tilde{\nabla}^2 \tilde{\mathbf{u}} - \frac{r_0}{H} \tilde{\rho}\, \hat{\mathbf{z}} + 2\tilde{\mathcal{C}} (\tilde{v}\hat{\mathbf{x}} - \tilde{u}\hat{\mathbf{y}}) \,, \tag{1}$$

$$\tilde{\nabla} \cdot \tilde{\mathbf{u}} = 0 \,, \tag{2}$$

$$\frac{\partial \tilde{\rho}}{\partial \tilde{t}} + \tilde{\mathbf{u}} \cdot \tilde{\nabla} \tilde{\rho} = \frac{1}{\mathrm{Re\,Sc}} \tilde{\nabla}^2 \tilde{\rho} \,. \tag{3}$$

Here, $\tilde{\mathbf{u}} = \{\tilde{u}, \tilde{v}, \tilde{w}\}$ is the dimensionless velocity, $\tilde{p}$ the dimensionless pressure and $\tilde{\rho}$ the dimensionless density given by $\tilde{\rho} = (\rho - \rho_0) \,/\, (\rho_1 - \rho_0)$ where ρ is the local fluid density. The last term on the right hand side of Equation (1) accounts for the effect of rotation, i.e. the Coriolis force. The centrifugal force has been absorbed into the pressure term. Dimensionless variables for Equations (1)–(3) are defined with length scale r_0, velocity scale $U = \sqrt{RgH}$ with $R = (\rho_1 - \rho_0)/\rho_0$, time scale $T = r_0/U$ and pressure scale $\rho_0 U^2$. The gravitational acceleration is $\mathbf{g} = -g\,\hat{\mathbf{z}}$. Using the former time scale implies the assumption that the local time scale is equal to the advective time scale in the momentum balance. The dimensionless parameters in Equations (1)–(3) are the Reynolds, Schmidt and Coriolis numbers defined as, respectively,

$$\mathrm{Re} = \frac{U\,H}{\nu} \,, \quad \mathrm{Sc} = \frac{\nu}{\kappa} \quad \text{and} \quad \tilde{\mathcal{C}} = \frac{\Omega_z\, r_0}{U} . \tag{4}$$

Here ν is the kinematic viscosity and κ the molecular diffusivity of the scalar property that changes the density of the fluid. The remaining parameter r_0/H is the aspect ratio characterising the initial conditions.

The governing Equations (1)–(3) are solved in a periodic dimensionless rectangular box of size $\tilde{L}_x \times \tilde{L}_y \times \tilde{H}$. For all simulations $\tilde{L}_x = \tilde{L}_y$ because the current spreads radially in the horizontal plane ($\tilde{x}$-$\tilde{y}$). A fully de-aliased pseudo-spectral code [35] is employed with

Fourier expansions along the horizontal directions $\tilde{x}$ and $\tilde{y}$ and a Chebyshev expansion with Gauss–Lobatto quadrature points along the vertical direction $\tilde{z}$. The flow field is time advanced using a Crank–Nicolson scheme for the diffusion terms and a third-order Runge–Kutta scheme for advection terms. Advection terms in Equation (1) are handled with the Arakawa method [36]. The buoyancy term is also advanced with a third-order Runge–Kutta scheme.

Periodic boundary conditions are imposed at the lateral (vertical) boundaries for all variables. At the top wall we employ a 'free-slip' boundary condition for the velocity field ($\partial\tilde{\mathbf{u}}/\partial\tilde{z} = 0$) and a *zero-gradient* boundary condition for the density field ($\partial\tilde{\rho}/\partial\tilde{z} = 0$). At the bottom wall, different boundary conditions are employed for the velocity field (see Table 1 for details) and a *zero-gradient* boundary condition for the density field.

As an initial condition for the velocity field we imposed zero velocity in the entire domain. For the density field we start our simulations with the heavy fluid confined in a cylindrical region of radius r_0 and height H (blue area in Figure 2) surrounded by the lighter ambient fluid that occupies the rest of the domain. We added a small perturbation to the density field to ensure that the rectangular platform of the domain and the grid do not introduce any bias in the evolution of the front. The effect of the small random disturbances in the initial condition has been studied before by Cantero et al. [37], who used the same pseudo-spectral code as in this work. The density field was set up using an error function (Equation (9) in [37]). It is stated in that paper that 'the parameters used were selected to produce a decorrelated interface with a white noise energy spectrum'. Using this error function, we ensure that no artificially wavelength that could evolve in an artificial lobe and cleft pattern is selected.

A detailed description of the implementation and validation of the code can be found in [31] and [38]. The grid employed for every simulation is detailed in Table 1. The numerical resolution for each simulation was based on the experience of previous works [6,8,23,37] and selected to have between 6 and 8 decades of decay in the energy spectrum for all the variables. The time step was selected to produce a Courant number smaller than 0.5. For viscous rotating fluids, it is important to accurately capture the dynamics inside the so-called Ekman layer defined as $\delta_{\mathrm{Ek}} = \sqrt{\nu/\Omega_z}$ which can be written in dimensionless form as $\delta_{\mathrm{Ek}}/H = \sqrt{r_0/H}/\sqrt{\mathrm{Re}\,\tilde{C}}$. In the simulations reported here δ_{Ek}/H is about 2%–5%, and it is described by approximately 14 grid points. The simulations performed for this work were

Table 1. Numerical simulations performed for this work. The table shows the time at which the fronts reach the maximum distance of propagation for the first oscillation ($\tilde{t}_{\mathrm{max}}$), the maximum distance of propagation of the fronts ($\bar{r}_{\mathrm{max}}$), the radius of the lens ($\bar{r}_{\mathrm{lens}}$) and the frequency of the front oscillations ($\overline{\omega}_p$). 'B.C.' refers to the bottom boundary condition for velocity: 'F.S.' and 'N.S.' are 'free-slip' and 'no-slip' boundary conditions, respectively. All simulations have a 'free-slip' boundary condition at the top boundary and a Schmidt number $Sc = 1$.

Case	$\tilde{C}$	Re	$\tilde{L}_x \times \tilde{L}_y \times \tilde{H}$	$N_x \times N_y \times N_z$	B.C.	$\tilde{t}_{\mathrm{max}}$	$\bar{r}_{\mathrm{max}}$	$\bar{r}_{\mathrm{lens}}$	$\overline{\omega}_p$
1	0.1	4000	$18 \times 18 \times 1$	$960 \times 960 \times 128$	F.S.	19.9	7.2	6.3	0.19
2	0.15	4000	$15 \times 15 \times 1$	$768 \times 768 \times 128$	F.S.	15.8	5.7	5.3	0.30
3	0.25	4000	$15 \times 15 \times 1$	$768 \times 768 \times 128$	F.S.	11.3	4.2	4.1	0.50
4	0.15	4000	$15 \times 15 \times 1$	$768 \times 768 \times 128$	N.S.	17.6	4.5	4.7[a]	0.37
5	0.15	8000	$15 \times 15 \times 1$	$960 \times 960 \times 180$	N.S.	17.2	4.5	4.7[a]	0.32
6	0	8000	$15 \times 15 \times 1$	$960 \times 960 \times 180$	N.S.	—	—	—	—

[a]For these cases the radius of the lens continuously increases at very low velocity and the value reported corresponds to the end of the oscillation period at $\tilde{t} = 100$.

done in Intel Xeon E5-2660 CPUs processor with 16 cores and 64 GB of RAM. Each 75-million-grid-point simulation took approximately 40 days and produced 2.3 TB of data, while each 165-million-grid-point simulation took approximately 60 days and produced 4.8 TB of data.

3. Results and discussions

This work presents six simulations of cylindrical gravity currents with the geometrical configuration depicted in Figure 2. A detailed description of the cases studied is presented in Table 1. Cases (1)–(3) only differ in the Coriolis parameter, case (4) has a different boundary condition at the bottom ('no-slip'), and case (5) has a 'no-slip' bottom boundary condition and a higher Reynolds number (Re = 8000). Case (6) is a simulation for Re = 8000 without rotational effects. All simulations have a 'free-slip' boundary condition at the top boundary, an initial aspect ratio of the initial condition $r_0/H = 1$ and a Schmidt number Sc = 1. In the case of planar non-rotating currents, Bonometti and Balachandar [39] showed that the dynamics of the current is independent of the Schmidt number provided the Reynolds number is large. The effect of Schmidt number in rotating gravity currents will be addressed in a future manuscript. It is worth mentioning here, however, that the numerical results with Sc = 1 present reasonable agreement with experimental observations for saline currents for which Sc $\approx$ 700.

3.1. Front dynamics

Rotational effects have a large impact on the development of the flow. One of the most distinct effects is the inhibition of the flow to continuously spread. This well-known process is called geostrophic adjustment (see e.g. [32]). This section presents the dynamics of this process in the context of low Coriolis number from the point of view of detailed three-dimensional numerical simulations.

3.1.1. Shape and front evolution during geostrophic adjustment

Figure 6 shows mean density iso-surfaces for case (3) at several times: $\tilde{t} = 2.5, \tilde{t} = 5, \tilde{t} = 10$ and $\tilde{t} = 20$. Initially the current spreads as in the absence of rotation. Detailed description and explanation of the dynamics of cylindrical gravity currents in the absence of rotation can be found in Cantero et al. [8]. As the flow develops, the Coriolis force becomes stronger and eventually becomes a dominant force.

Figure 6 shows the net effect of rotation on the spreading. For $\tilde{t} = 20$ the front has only advanced a distance of 0.1 as compared to $\tilde{t} = 10$. Eventually the front reaches a final steady lens shape (free-slip conditions) or quasi-steady lens shape (no-slip condition). The lens shape for $\tilde{t} = 20$ in Figure 6 is representative of the final current shape.

A local equivalent height $\overline{h}$ is defined for the computation of the maximum distance of front propagation. Shin et al. [40] and Marino et al. [13] defined a local equivalent height in an unambiguous way as

$$\tilde{h}(\tilde{r}, \tilde{\theta}, \tilde{t}) = \int_0^{\tilde{H}} \tilde{\rho}\, d\tilde{z}\,, \tag{5}$$

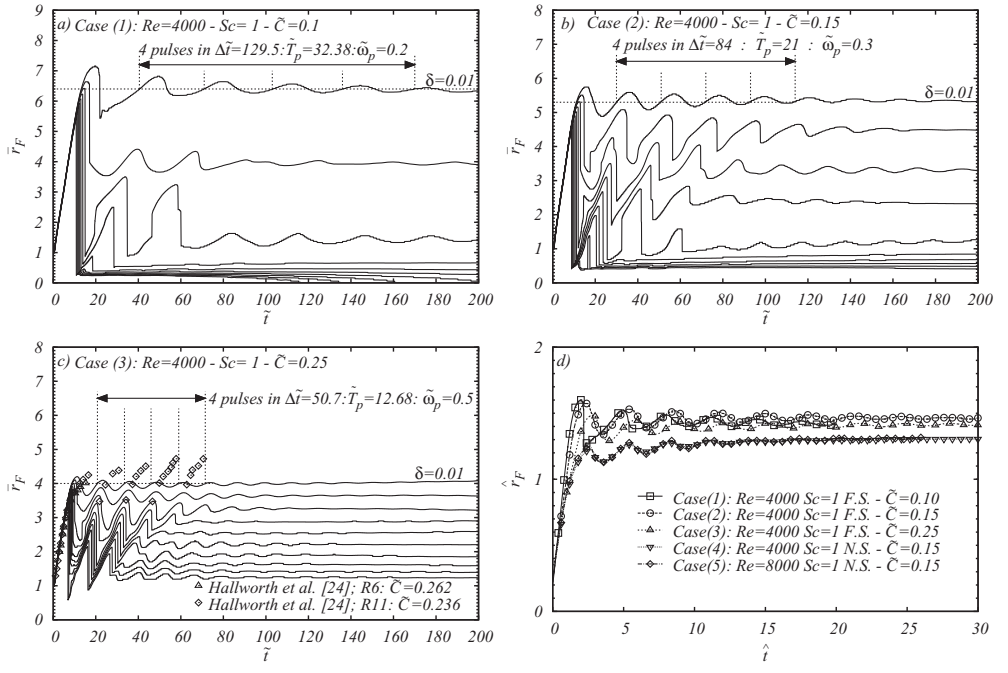

Figure 3. Front location $\overline{r}_F$ as a function of time $\tilde{t}$ for different thresholds of $\overline{h}$, from $\delta = 0.01$ to $\delta = 0.1$, for (a) case (1), (b) case (2), (c) case (3), (d) cases (1)–(5) with scaling $\hat{t} = \Omega_z t$ and $\hat{r}_F = r\tilde{C}^{1/2}/r_0$. Experimental observations by Hallworth et al. [24] are for $\mathrm{Re} = 2.09 \times 10^5$ (R11) and $\mathrm{Re} = 2.93 \times 10^5$ (R6), $\tilde{C} = 0.24$ (R11) and $\tilde{C} = 0.26$ (R6) and $\mathrm{Sc} = 700$.

$\tilde{r}$ being the radial position and $\tilde{\theta}$ the azimuthal position. At locations where the entire layer is occupied by the heavy fluid, the equivalent height is unity, whereas at locations where the light fluid fills the entire layer, the equivalent height $\tilde{h}$ is zero. The local current height can then be averaged over the azimuthal direction. The mean equivalent height is defined as

$$\overline{h}(\tilde{r}, \tilde{t}) = \frac{1}{2\pi} \int_0^{2\pi} \tilde{h}(\tilde{r}, \tilde{\theta}, \tilde{t})\, d\tilde{\theta}\,. \tag{6}$$

The mean front location $\overline{r}_F$ can now be defined as the radial position where the mean equivalent height $\overline{h}$ becomes smaller than a small threshold δ. Precise definition can be found in Cantero et al. [23]. Mean flow variables are computed as

$$\overline{f}(\tilde{r}, \tilde{z}, \tilde{t}) = \frac{1}{2\pi} \int_0^{2\pi} \tilde{f}(\tilde{r}, \tilde{\theta}, \tilde{z}, \tilde{t})\, d\tilde{\theta}\,, \tag{7}$$

where $\tilde{f}$ can be the density field or the velocity field.

Figure 3(a–c) shows the front location $\overline{r}_F$ as a function of time for cases (1)–(3) and for different threshold values of $\overline{h}$. The upper curve corresponds to the threshold $\delta = 0.01$. The threshold $\delta = 0.01$ captures adequately the dynamics of the front in agreement with flow visualisations and it is used for the computation of front locations reported in this work.

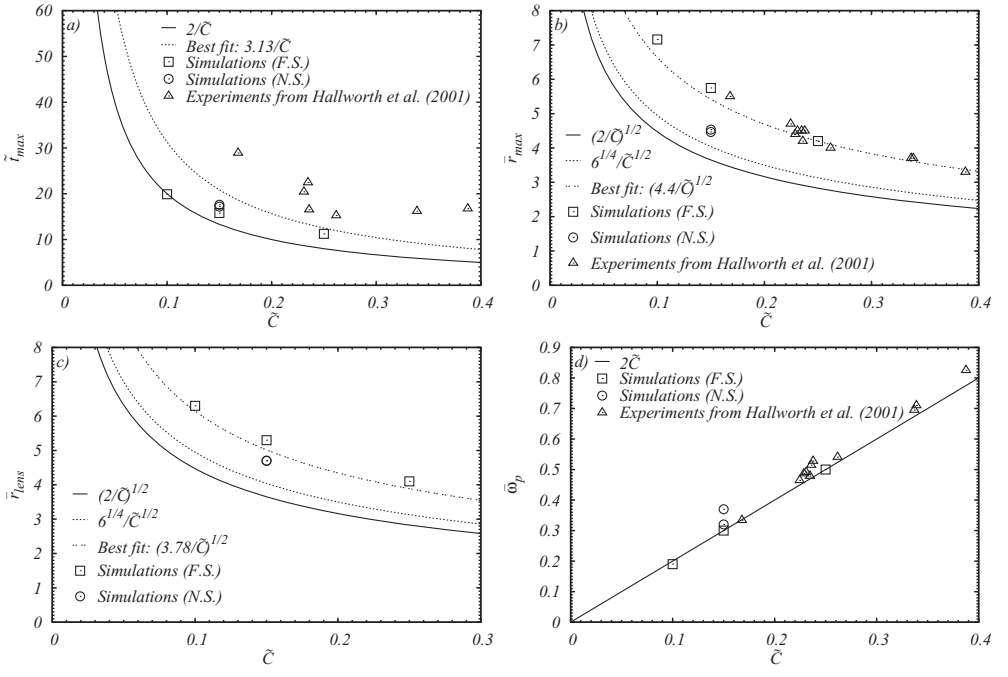

Figure 4. Comparison of numerical results with experimental observations and theoretical predictions (see also Table 1). Experimental observations by Hallworth et al. [24] are for $\mathrm{Re} = 2.09 \times 10^5$ (R11) and $\mathrm{Re} = 2.93 \times 10^5$ (R6), $\tilde{\mathcal{C}} = 0.24$ (R11) and $\tilde{\mathcal{C}} = 0.26$ (R6) and $\mathrm{Sc} \approx 700$. (a) Time at which the fronts reach the maximum distance of propagation for the first oscillation $\tilde{t}_{\mathrm{max}}$. Solid line: empirical law obtained from shallow-water simulations [28]. (b) Maximum distance of propagation of the fronts $\tilde{r}_{\mathrm{max}}$. Solid line: shallow-water solution for the steady-state lens in the case $\tilde{\mathcal{C}} \ll 1$ [28]. Dotted line: Box-model solution [29]. (c) Radius of the lens $\tilde{r}_{\mathrm{lens}}$. The solid and dotted lines are the same as in frame *b*. (d) Frequency of the front oscillations $\tilde{\omega}_p$. Solid line: empirical law obtained in the experiments of Hallworth et al. [24].

For all cases reported in Figure 3(a–c) the front moves outward for some time, until the front velocity becomes zero, and then the current starts to move inward. This process is repeated for several cycles. The dynamics of the front can also be observed in the video supplied as supplementary material SupMatVideo1.avi. The first oscillation peak occurs at $\tilde{t}_{\mathrm{max}} \approx 19.9$, $\tilde{t}_{\mathrm{max}} \approx 15.8$ and $\tilde{t}_{\mathrm{max}} \approx 11.3$, for cases (1)–(3), respectively (see Table 1). These times are in agreement with results reported by Ungarish [28] using a shallow water model, where the maximum radius of the current occurs at $\tilde{t}_{\mathrm{max}} \sim 2/\tilde{\mathcal{C}}$ (for $\tilde{\mathcal{C}} \ll 1$). This comparison is shown in Figure 4(a) together with experimental data from Hallworth et al. [24]. These experimental data are also included in Figure 3(c) and present two distinct aspects worth mentioning here. First, every new front oscillation reaches further away and, second, there is a time delay of the experimental data with respect to the simulation results. Note that the dimensionless numbers of the flow in our numerical simulations are noticeably different from those assumed in the laboratory.

Experimental data from Hallworth et al. [24] are for $\mathrm{Re} = 2.09 \times 10^5$ (run R11) and $\mathrm{Re} = 2.93 \times 10^5$ (R6), $\tilde{\mathcal{C}} = 0.24$ (run R11) and $\tilde{\mathcal{C}} = 0.26$ (run R6), and $\mathrm{Sc} = 700$. Results of Cantero et al. [23] show that the effect of Reynolds number on the front velocity of density currents is minor as long as it is larger than $\mathrm{Re} \approx 4000$. Furthermore, Bonometti et al. [39]

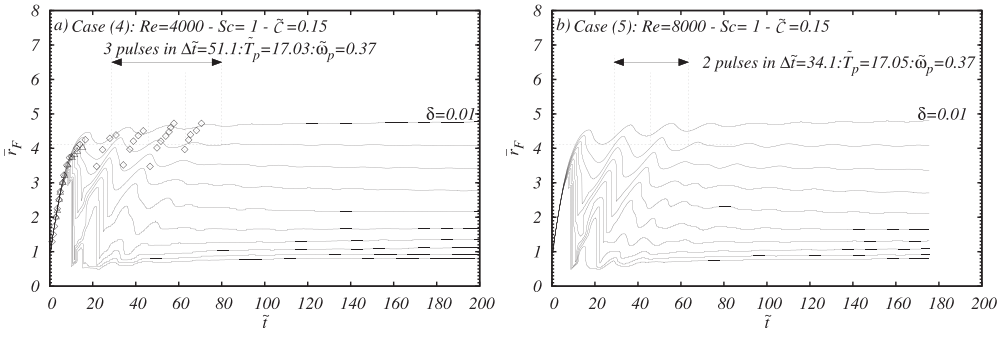

Figure 5. Effect of the Reynolds number. Front location $\bar{r}_F$ as a function of time $\tilde{t}$ for different thresholds of $\bar{h}$, from $\delta = 0.01$ to $\delta = 0.1$, for (a) case (4) and (b) case (5). Experimental observations by Hallworth et al. [24] for which Sc = 700: open squares (R11), Re = 2.09×10^5, $\tilde{C} = 0.24$; open triangles (R6), Re = 2.93×10^5, $\tilde{C} = 0.26$.

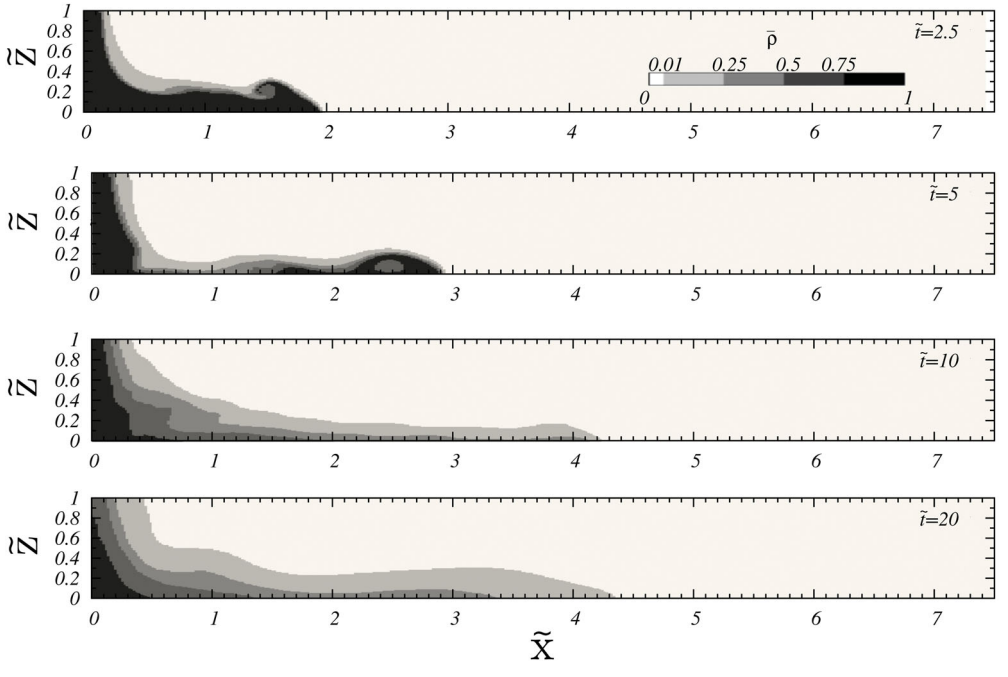

Figure 6. Mean density iso-surface contours for case (3). The sequence shows the time development of the current. The current shape for $\tilde{t} = 20$ is representative of the steady state shape.

show that a variation from Sc = 1 to Sc = $O(10^3)$ at Re ≈ 10000 leads to a variation of the front velocity of ≈5%. Although Cantero et al.'s [23] and Bonometti et al.'s [39] results are for non-rotating currents, it is assumed that their findings remain valid for the low Coriolis number currents used in this work and thus that the comparison between the present numerical results with the experiments of Halwworth et al. [24] is relevant. In view of these observations, the discrepancies between numerical results and experimental observations in Figures 3(c) and 4(a) can be mainly attributed to the different bottom boundary conditions between experiments and numerical simulations for cases (1)–(3). Figure 3(d) shows

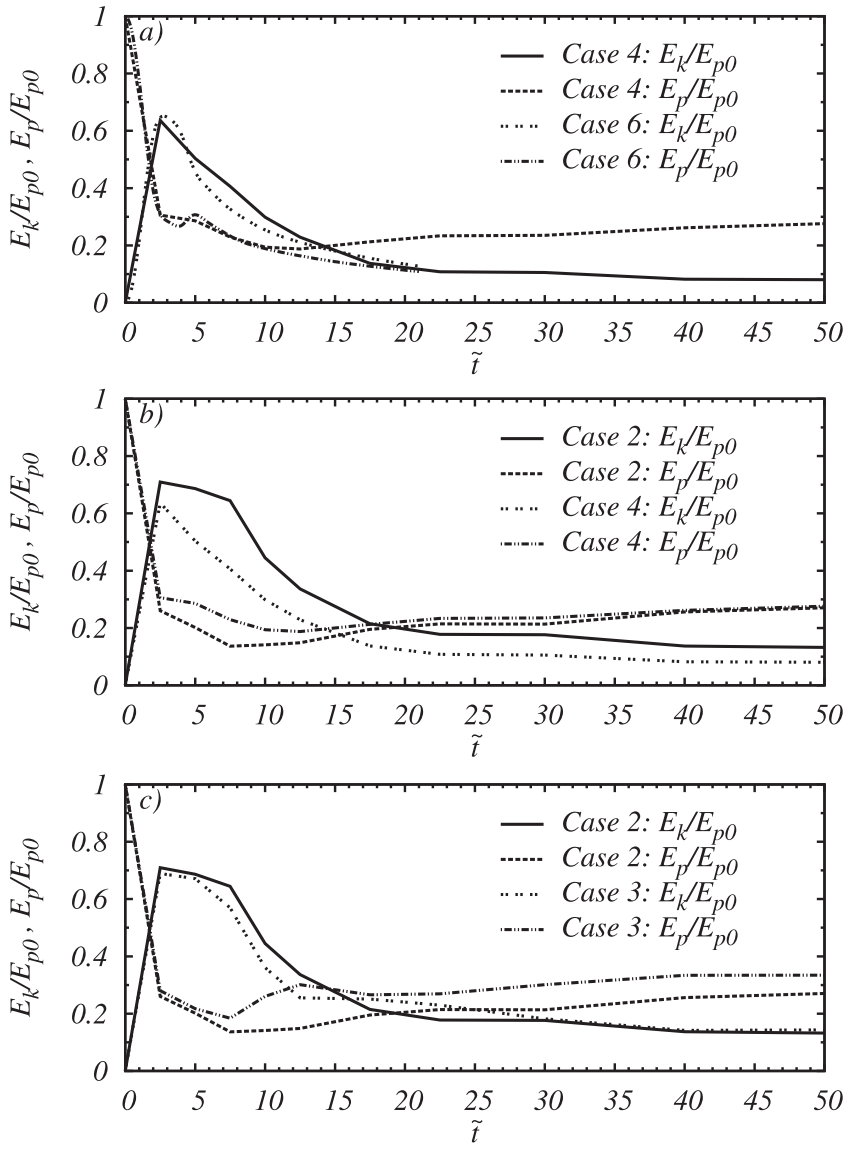

Figure 7. (a) Time evolution of kinetic energy E_k and potential energy E_p scaled with the initial potential energy E_{p0} for: (a) cases (4) and (6); (b) cases (2) and (4); (c) cases (2) and (3).

the front location for cases (1)–(5) employing scales $1/\Omega_z$ for time and $r_0/\tilde{\mathcal{C}}^{1/2}$ for length giving dimensionless variables $\hat{t}$ and $\hat{r}_F$. Reasonable collapse of the results is obtained for these scales for each type of boundary condition. Figure 4(a) clearly shows the differences in front spreading for cases (4) and (5) with 'no-slip' as compared to cases (1)–(3) with 'free-slip'. Table 1 reports the delay on $\tilde{t}_{\max}$ for cases (4) and (5) with respect to case (2).

At the first oscillation, the current reaches the maximum distances of propagation as can be observed in Figure 3(a–c). These values are reported in Table 1 and are $\bar{r}_{\max} \approx 7.2$, $\bar{r}_{\max} \approx 5.7$ and $\bar{r}_{\max} \approx 4.2$, for cases (1)–(3), respectively. The larger the Coriolis number

the shorter the maximum propagation distance (see Section 3.1.2). Numerical solution of the shallow water model and box model approximations [30] predict $\overline{r}_{\max} = 6.1$ and $\overline{r}_{\max} = 5.0$, respectively, for $\tilde{\mathcal{C}} = 0.1$. These model predictions differ from our results by 15% and 30%, respectively. Experimental observations by Hallworth et al. [24] show values of $\overline{r}_{\max} = 4.3$ and $\overline{r}_{\max} = 4$ for $\tilde{\mathcal{C}} = 0.24$ and $\tilde{\mathcal{C}} = 0.26$, respectively (experiments R11 and R6 in [24]). This comparison is shown in Figure 4(b).

After several cycles of oscillation the flow reaches eventually steady state for cases (1)–(3), for which the front spreading stops and the current assumes a lens shape. As a consequence of bottom 'no-slip' boundary condition (see Section 3.1.2), cases (4) and (5) continue to spread outward for all times at a very low speed. Figure 8 shows the current shape for case (2). Figure 8(a,b) shows the mean density field $\overline{\rho}$ for two time instances: $\tilde{t} = 15.8$ corresponding to the time when the current reaches the maximum distance of propagation (first peak in Figure 3(b) for threshold $\delta = 0.01$) and $\tilde{t} = 100$ corresponding to a time long enough for which front oscillations are small. For $\tilde{t} > 100$ the front location displays oscillations below 5% and the final lens shape of the current can be assumed to have been achieved. This shape is clearly seen in Figure 8(d) for $\tilde{t} = 100$, which shows a density iso-surface of $\tilde{\rho} = 0.01$. The lens shape of the current at the steady state is in agreement with experimental observations and shallow water models for rotating cylindrical gravity currents [24]. This profile is known as 'nose down' because the head height becomes small in the steady state. This type of profile is not seen in gravity currents without rotation [8]. Comparing Figures 8(c) ($\tilde{t} = 15.8$) and 8(d) ($\tilde{t} = 100$) we can see a small difference in the lens radius, although the three-dimensional shape of the lens is different (more turbulent structures that modify the interface at time $\tilde{t} = 15.8$).

The steady state lens mean radius $\overline{r}_{\text{lens}}$ is also influenced by the Coriolis parameter, in particular $\overline{r}_{\text{lens}} = 6.3$, $\overline{r}_{\text{lens}} = 5.3$ and $\overline{r}_{\text{lens}} = 4.1$ for cases (1)–(3), respectively. The values are also reported in Table 1. Analytic approximations of the shallow water equations [28] predict steady state lens radius of $\overline{r}_{\text{lens}} = 4.5$, $\overline{r}_{\text{lens}} = 3.7$ and $\overline{r}_{\text{lens}} = 2.8$ for $\tilde{\mathcal{C}} = 0.1$, $\tilde{\mathcal{C}} = 0.15$ and $\tilde{\mathcal{C}} = 0.25$, respectively. These values differ by 30% from the numerical results. This comparison is shown in Figure 4(c).

The front oscillatory behaviour until the flow reaches the steady state lens shape can be characterised by the mean oscillation period $\overline{T}_p$. The mean oscillation period for each simulation is defined as the averaged time interval on which the successive outward fronts tracked by $\overline{h}$ and the threshold $\delta = 0.01$ reach $\overline{r}_{\text{lens}}$ (see Figure 3). The mean oscillation frequency $\overline{\omega}_p$ is defined as $\overline{\omega}_p = 2\pi / \overline{T}_p$. Values of $\overline{\omega}_p$ for all simulations are shown in Table 1. For cases (1)–(3), these values satisfy the empirical linear relation $\overline{\omega}_p \approx 2\tilde{\mathcal{C}}$. Similar laboratory observations are reported for cylindrical gravity currents by Hallworth et al. [24]. These are shown in Figure 4(d).

3.1.2. *Mean flow dynamics and the effect of bottom boundary condition*

In the absence of rotation, gravity currents spread radially transitioning through different phases of spreading [23]. The rotation of the system modifies substantially this global behaviour of gravity currents. As explained in Section 3.1, the flow develops initially as if there were no rotation on the system [8], but eventually it feels the effect of the Coriolis force and retreats inwards. For the cylindrical coordinates shown in Figure 2 the mean Coriolis

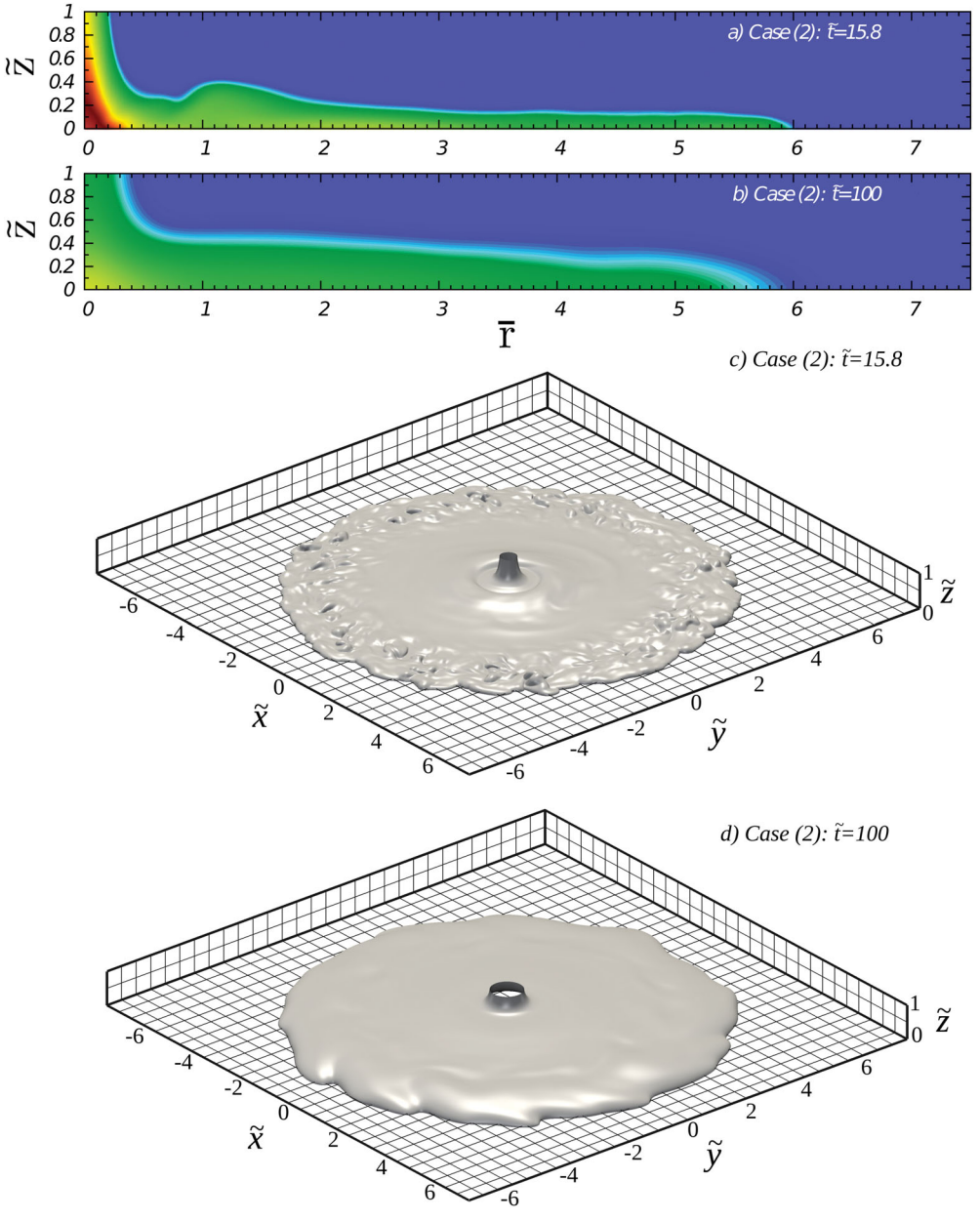

Figure 8. (a) Density field $\overline{\rho}$ at $\tilde{t} = 15.8$, for case (2); (b) density field $\overline{\rho}$ at $\tilde{t} = 100$, for case (2); (c) Lens shape at $\tilde{t} = 15.8$ visualised by an iso-surface of density $\tilde{\rho} = 0.01$, for case (2); (d) steady state lens shape at $\tilde{t} = 100$ visualised by an iso-surface of density $\tilde{\rho} = 0.01$, for case (2).

force may be written as

$$-2\tilde{\mathcal{C}}\hat{\mathbf{z}} \times \overline{\mathbf{u}} = 2\tilde{\mathcal{C}}\left(\overline{u}_t\,\hat{\mathbf{r}} - \overline{u}_r\,\hat{\mathbf{t}}\right), \tag{8}$$

where $\overline{u}_r$ and $\overline{u}_t$ are the mean radial and mean tangential velocities, respectively.

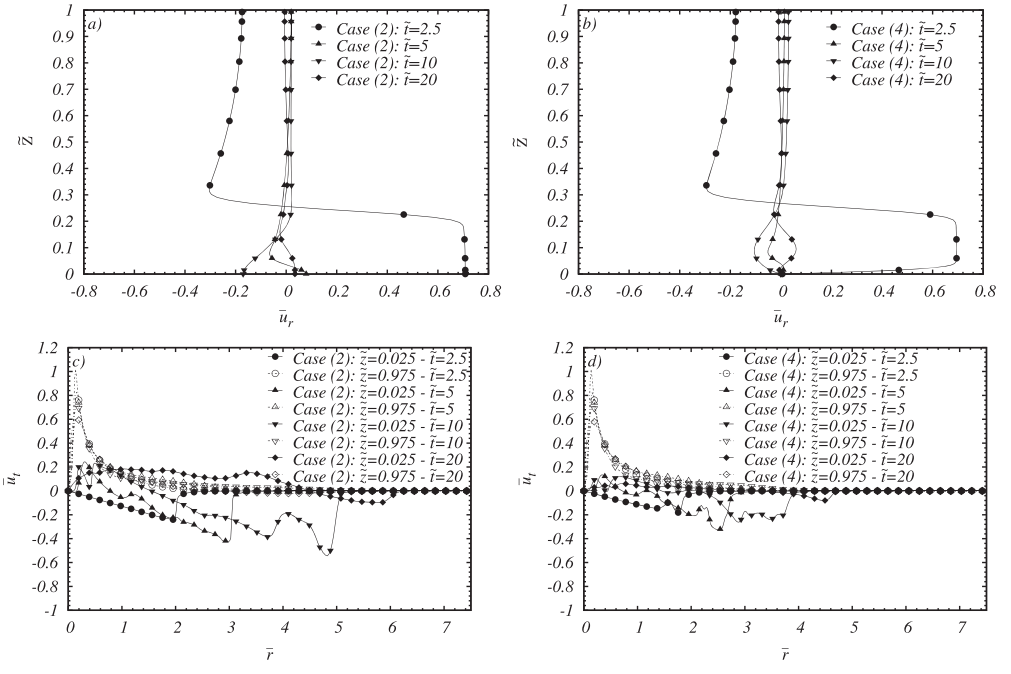

Figure 9. Effect of the bottom friction on the span-averaged velocity profiles. Mean radial velocity $\overline{u}_r$ as a function of $\tilde{z}$ at $\overline{r} = 1$ for (a) case (2) and (b) case (4). Mean tangential velocity $\overline{u}_t$ as a function of $\overline{r}$ at $\tilde{z} = 0.025$ and $\tilde{z} = 0.975$ for (c) case (2) and (d) case (4).

Mean radial velocity profiles ($\overline{u}_r$) as a function of $\tilde{z}$ for $\overline{r} = 1$ are presented in Figure 9(a) for case (2). Figure 9(c) shows the mean tangential velocity profiles ($\overline{u}_t$) as a function of the radial position $\overline{r}$ for case (2) for vertical locations $\tilde{z} = 0.025$ and $\tilde{z} = 0.975$. When the heavy fluid is released and starts to move in the positive radial direction as a result of the buoyancy force, a Coriolis force in the negative tangential direction develops as seen in Equation (8). The tangential Coriolis force induces flow in this direction. This effect can be seen in Figure 9(a) for $\tilde{t} = 2.5$, where a velocity in the positive radial direction $\overline{u}_r \approx 0.7$ produces a Coriolis force component in the negative tangential direction which induces a velocity $\overline{u}_t \approx 0.24$ in the negative tangential direction at the front (see Figure 9(c) for $\tilde{z} = 0.025$ and $\tilde{t} = 2.5$ at $\overline{r} \approx 2$). Consequently, a Coriolis force component in the negative radial direction develops, which interacts with the buoyancy force. For $\tilde{t} = 5$ the current has felt the effect of the Coriolis force and the flow has started to retreat as seen in Figure 9(a) where the current velocity is negative for $0.04 < \tilde{z} < 0.45$. At $\tilde{t} = 10$ the Coriolis force has acted strongly on the flow and the body of the current is moving in the negative radial direction as seen in Figure 9(a). At $\tilde{t} \approx 20$ the second inertial oscillation of the front occurs (see Figure 3(b) for $\tilde{t} \approx 20$). This flow in the positive radial direction produces again a Coriolis force in the negative tangential direction, and the process described above repeats itself for several cycles. The oscillatory process described is the well-known dynamics of inertial oscillations in the adjustment to geostrophy. At $\tilde{t} \approx 100$, the amplitude of the front location oscillations drops significantly, and the current acquires the final lens shape similar to the one seen in Figure 8(d) (geostrophic adjustment). At this time the mean radial velocity $\overline{u}_r$ is practically zero. Figure 9(c,d) displays also large values of positive tangential velocity for

$0 < \tilde{r} < 2$ close to the top boundary. This is a consequence of the negative radial velocity that develops close to the top boundary forced by mass conservation and the outward moving front in the bottom part of the domain. A negative radial velocity induces a positive tangential Coriolis force. The dynamics described before for mean flow can also be observed in the video supplied as supplementary material SupMatVideo1.avi.

Cases (4) and (5) only differ by the value of the Reynolds number. Figure 5(a,b) shows the front location for cases (4) and (5), respectively, as a function of time and for different thresholds values of $\overline{h}$. As can be observed in this figure, there is no major influence of the Reynolds number for the range studied. The same conclusion can be drawn from other parameters and we have decided no to show them here. On the other hand, the bottom boundary condition influences quantities such as $\overline{r}_{\max}$, $\overline{r}_{\text{lens}}$ and $\overline{\omega}_p$ [41].

The effect of the bottom boundary condition can be addressed by comparing cases (2) and (4), which differ only on the bottom boundary condition: case (2) with a 'free-slip' and case (4) with 'no-slip'. Figure 5(a) shows that the maximum distances of propagation of the front $\overline{r}_{\max}$ is smaller than for case (2) (see Figure 3(d) and also Table 1 where $\overline{r}_{\max} = 5.7$ and $\overline{r}_{\max} = 4.5$ for cases (2) and (4), respectively). This is consistent with the fact that the flow in the radial direction for case (4) is further restricted by bottom shear owing to the 'no-slip' bottom boundary condition. This difference can also be seen by comparing Figure 9(a,b), where vertical profiles of $\overline{u}_r$ are presented for radial position $\tilde{r} = 1$ for cases (2) and (4), respectively. At $\tilde{t} = 2.5$ the positive radial velocity for $\tilde{z} < 0.04$ for case (4) is smaller than for case (2), producing a weaker Coriolis force in the negative tangential direction. Thus smaller negative tangential velocities of the flow are induced and, consequently, a weakened Coriolis force in the negative radial direction. This produces the smaller inward radial velocities seen in Figure 9(b) for times $\tilde{t} = 5$ and $\tilde{t} = 10$ as compared to Figure 9(a).

Another distinctive effect of the 'no-slip' bottom boundary condition is that the maximum radius of the successive outward fronts are not smaller than in the previews oscillations (compare Figure 3(b) and Figure 5(a)). This behaviour was observed by Hallworth et al. [24] in laboratory experiments and is not seen in case (2) with a 'free-slip' boundary condition at the bottom. Experimental data from Hallworth et al. [24] for $\tilde{C} \approx 0.25$ is included in Figure 5(a). This difference in behaviour as a result of the boundary condition can be explained by analysing Figure 9(c,d), which present mean tangential velocity radial profiles ($\overline{u}_t$) for $\tilde{z} = 0.025$ and $\tilde{z} = 0.975$ for cases (2) and (4), respectively.

As explained earlier, the lower positive radial velocities for case (4) produce a weaker Coriolis force in the negative tangential direction and smaller tangential velocities. These lower tangential velocities produce weaker Coriolis forces in the negative radial direction, allowing the maximum distance achieved for each oscillation to be greater than the previous one. At later times ($\tilde{t} > 80$), the Coriolis force in the negative radial direction cannot balance the buoyancy force and the steady state is never reached for bottom 'no-slip' currents. A lens shape of the interface between the light and heavy fluid is observed however, but with an increasing $\overline{r}_{\text{lens}}$ over time. At this stage, the front advances at a velocity of the order of $\overline{u}_F = 10^{-4}$ for $80 < \tilde{t} < 200$, representing a variation of 1% of the front position. Also, a slight increase in the frequency of the successive outward fronts $\overline{\omega}_p$ is observed in case (4) as seen in Figure 5 and reported in Table 1. The effect of bottom boundary condition on mean flow can also be observed in the video supplied as supplementary material SupMatVideo2.avi.

Following the work of Necker et al. [42] we compute the kinetic energy E_k and potential energy E_p:

$$E_k(t) = \int_{\mathcal{V}} \frac{1}{2}(\tilde{\mathbf{u}} \cdot \tilde{\mathbf{u}})\, dV, \qquad E_p(t) = \int_{\mathcal{V}} \tilde{\rho} \cdot \hat{\mathbf{z}}\, dV, \tag{9}$$

where $\mathcal{V}$ is the entire domain. The Coriolis term does not contribute to the global energy balance. Figure 7 shows the time evolution of kinetic energy E_k and potential energy E_p scaled with the initial potential energy E_{p0}. In Figure 7(a) we compare case (6) (zero Coriolis number) with case (4) (non-zero Coriolis number). Both simulations have the same bottom boundary condition ('no-slip'). We can see a good agreement between both simulations for early times, when rotation effects are small. The effect of the bottom boundary condition is observed in Figure 7(b), which presents results for cases (2) and (4). These cases differ only through the bottom boundary condition. It can be clearly seen that the 'no-slip' boundary condition restricts the motion of the current, producing lower values of kinetic energy E_k/E_{p0} for times $\tilde{t} \gtrapprox 2$. Moreover, the kinetic energy seems to reach a constant value after $\tilde{t} \gtrapprox 40$ when the steady-state lens shape is achieved. The kinetic energy corresponds to azimuthal flow motion. Figure 7(b) also shows that the potential energy E_p/E_{p0} is larger for case (4) ('no-slip') at early times. The effect of boundary condition on the potential energy tends to be smaller for later times. After the first oscillation (see $\tilde{t}_{\max}$ at Table 1) potential energy increases and show an oscillatory behaviour as a result of flow contraction. This is clearly seen in Figure 7(c), which shows results for cases (2) and (3) with 'free-slip' boundary condition. After the initial acceleration phase and before $\tilde{t} \lessapprox 16$ the kinetic energy is lower for case (3) with the highest rotational effect. This is the result of the stronger restriction in the radial motion of the current. At later times when the currents reaches the steady state, the kinetic energy is larger for case (3) produced by the larger azimuthal velocities. It is interesting to see in Figure 7(c) that the increase in potential energy after the first oscillation of the front is larger as the rotational effect increases. At later times, the potential energy is larger for case (3), as the same initial density excess in both simulations is restricted to a lens of smaller radius in case (3).

3.2. Evolution of three dimensional flow structures

Rotational effects generate distinctive turbulent structures not present in the absence of rotation. Figure 10(a) shows the three-dimensional structure of the interface for case (2) described by an iso-surface of density $\tilde{\rho} = 0.05$ for time $\tilde{t} = 7.5$. Also shown in this figure are contours of density in the plane $\tilde{y} = 0$ (gray contours). Figure 10(b) shows the iso-surface of 'swirling strength' $\tilde{\lambda}_{ci} = 4$ for the same case and time. The 'swirling strength' is the absolute value of the imaginary portion of the complex eigenvalues of the local velocity gradient $\tilde{\nabla}\tilde{\mathbf{u}}$, and gives a means to determine the compactness of the vortical structures of the flow [43,44].

Figure 10(a) shows that the body of the current has azimuthal nominal symmetry, while the interface at the head of the current is highly influenced by vertical Kelvin–Helmholtz vortices identified as *KH*2 in Figure 10(b) surrounding the main horizontal Kelvin–Helmholtz vortex core *KH*1. Similar structures were observed by Ungarish et al. [29] in laboratory experiments. Hallworth et al. [24] mention the existence of some sort of instabilities at the front but they did not describe them in detail.

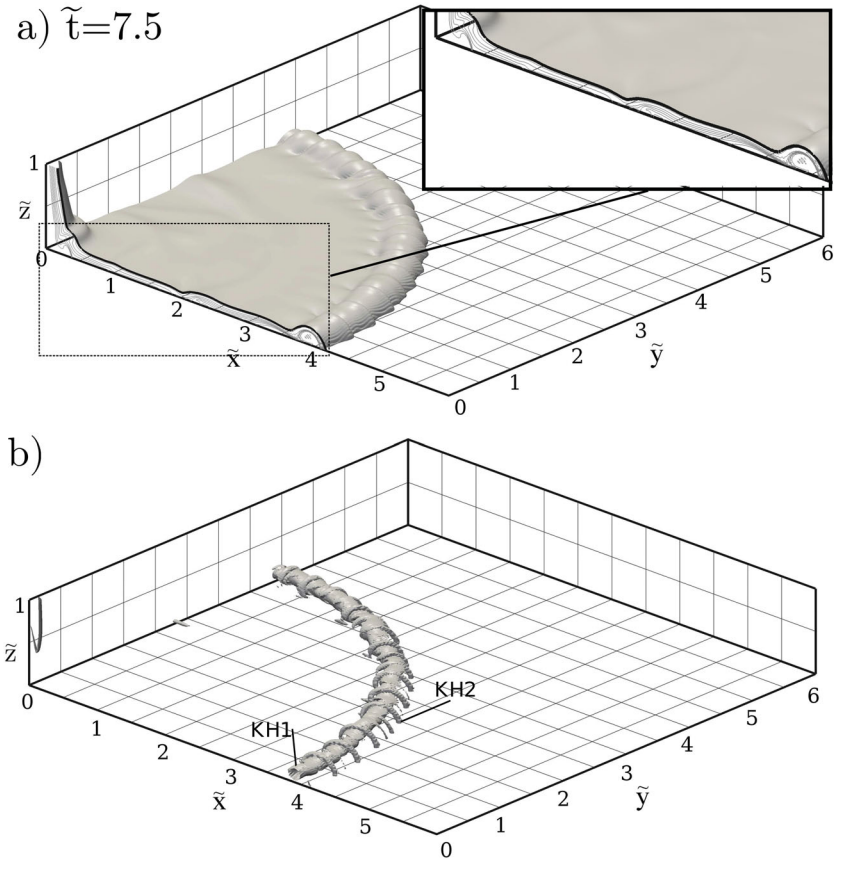

Figure 10. (a) Three-dimensional structure of the interface for case (2) visualised by an iso-surface of density $\tilde{\rho} = 0.05$ for $\tilde{t} = 7.5$. Also shown in this figure are density contours for plane $\tilde{y} = 0$ (gray contours in inset figure). (b) Iso-surface of swirling strength $\tilde{\lambda}_{ci} = 4$ for same case and time.

The effect of rotation on the three-dimensional structure of the currents for case (2) can be seen in the video supplied as supplementary material SupMatVideo3.avi. The vortex structures developed at the front of the current for case (2) can be seen in the video supplied as supplementary material SupMatVideo4.avi.

The turbulent structures that form in the current are richer in the case of 'no-slip' bottom boundary condition and high Reynolds number. The influence of rotation on the three-dimensional structure of the currents is thus analysed for case (5) with the highest Reynolds number simulated (Re = 8000) and with 'no-slip' bottom boundary condition. A stereoscopic three-dimensional view (in side-by-side format) of the flow dynamics for case (5) can be seen in the video supplied as supplementary material SupMatVideo5.avi.

Figures 11 and 12 show the time evolution of a composed view of the three-dimensional structure of the interface between the light and heavy fluids and the swirling strength $\tilde{\lambda}_{ci}$. The interface is visualised by the density field and turbulent structures by the swirling strength. Several turbulent structures are identified in these figures and can be followed over time. The evolution of the flow structures identified in Figures 11 and 12 can be seen in the video supplied as supplementary material SupMatVideo6.avi.

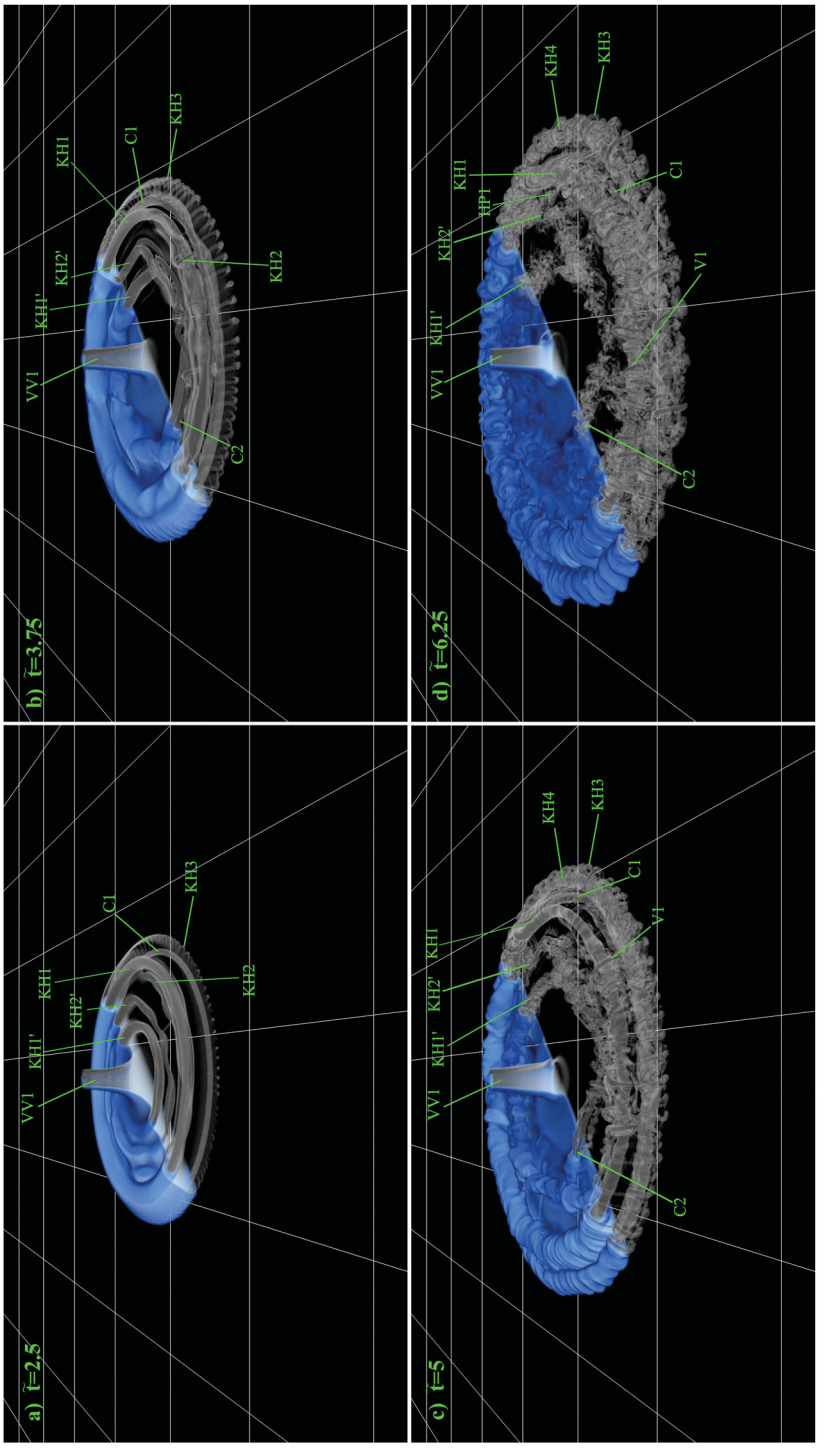

Figure 11. Three-dimensional structure for case (5) visualised by volume rendering of density $\tilde{\rho}$ (blue shaded region in the back-facing half of the domain) and turbulent structures visualised by volume rendering of swirling strength $\tilde{\lambda}_{ci}$ (gray shaded region in the front-facing half of the domain) for times (a) $\tilde{t} = 2.5$, (b) $\tilde{t} = 3.75$, (c) $\tilde{t} = 5$ and (d) $\tilde{t} = 6.25$. The dynamics of the structures shown in this figure can be observed in video SupMatVideo6.avi provided as supplementary material.

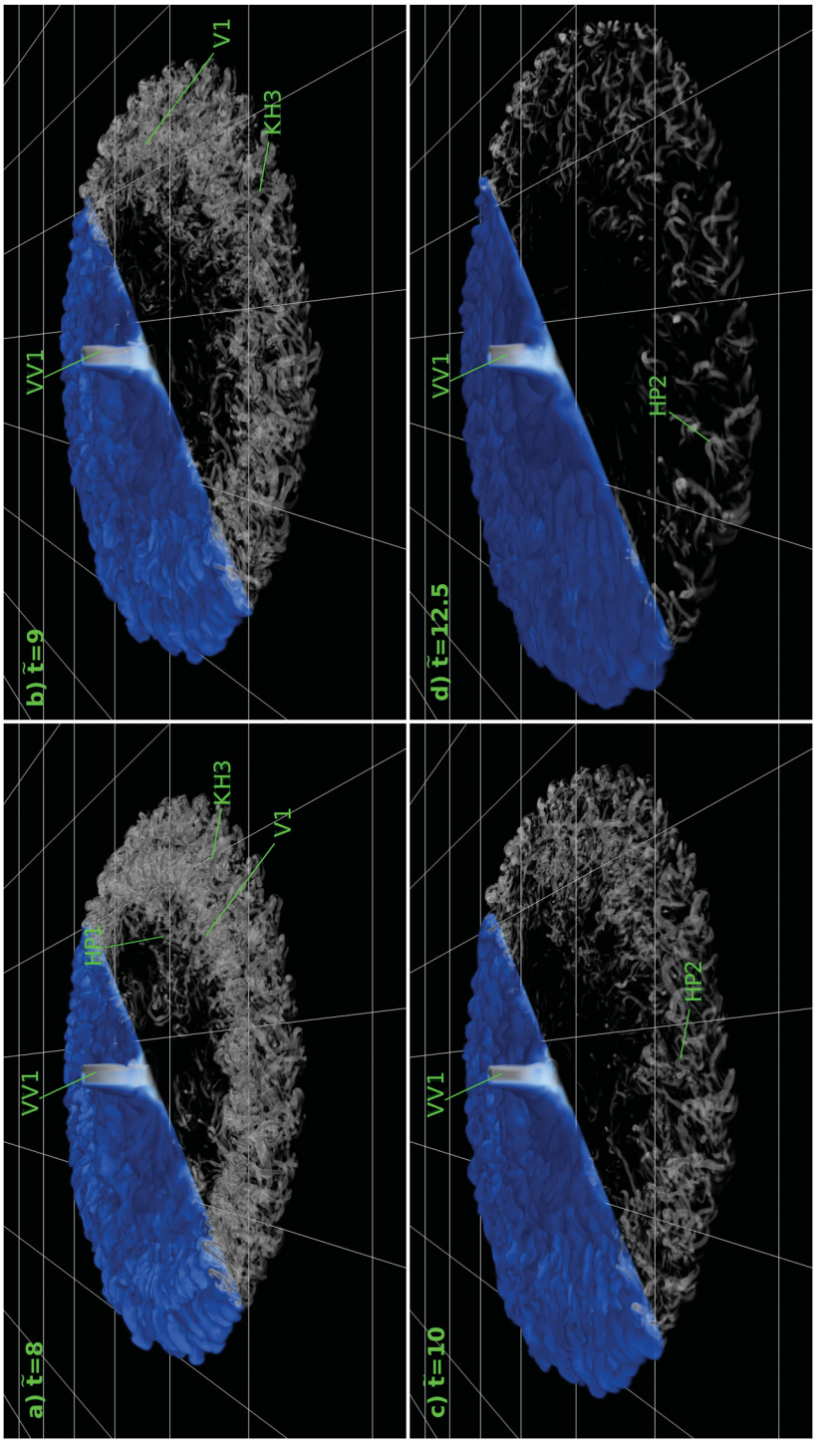

Figure 12. Same as Figure 11. (a) $\tilde{t} = 8$; (b) $\tilde{t} = 9$; (c) $\tilde{t} = 10$; (d) $\tilde{t} = 12.5$.

For $\tilde{t} = 2.5$ (Figure 11(a)) counter-clockwise rotating Kelvin–Helmholtz vortices *KH*1 and *KH*1′ have already formed during the first stages of development of the flow. The sense of rotation must be understood with the portion of the current spreading to the right. At this time secondary Kevin–Helmholtz vortices *KH*2 and *KH*2′ have also formed in between *KH*1 and *KH*1′. Vortex cores *KH*2′ and *KH*1′ stop their radial motion at $\tilde{t} \approx 5$ as a result of the Coriolis force in the negative radial direction. Figure 11(a) (for $\tilde{t} = 2.5$) also shows a clockwise-rotating vortex *C*1 forming at the bottom in front of vortex *KH*1 as a result of bottom shear stress. As a consequence of rotation, a vertical vortex core *VV*1 forms at the centre of the domain and an array of vertical Kelvin–Helmholtz vortices *KH*3 form at the front of the current. Vertical vortices *KH*3 are initially formed near the bottom as streamwise vortex cores and the vertical part develops later as the rotational effects increases.

At $\tilde{t} = 3.75$ (Figure 11(b)) almost all Kelvin–Helmholtz vortex cores seen in the picture start to twist and bend. At this time the interaction of vortex *KH*1 with *KH*2 and *KH*1′ with *KH*2′ starts. Also at this time, a new clockwise-rotating vortex *C*2 forms in front of vortex *KH*2′ at the bottom.

All Kelvin–Helmholtz instabilities are the result of shear. Kelvin–Helmholtz vortices *KH*1, *KH*1′, *KH*2 and *KH*2′ are the result of radial shear between the light and heavy fluids, and vortices *KH*3 are the result of tangential shear between the two fluids. This effect can be better seen in Figure 13(a), which is a composed view of the iso-surface of density $\tilde{\rho} = 0.05$ for time $\tilde{t} = 3.75$ with two slices of the density field: one for plane $\tilde{y} = 0$ and another for plane $\tilde{z} = 0.05$. Figure 13(b) shows a top view of the density in plane $\tilde{z} = 0.05$. The time evolution of the density top view in plane $\tilde{z} = 0.05$ can be seen in the video supplied as supplementary material SupMatVideo7.avi.

For $\tilde{t} = 5$ (Figure 11(c)) new toroidal vortices *KH*4 form between vortices *KH*3 at the front. The interaction of these vortices develops with *KH*3 vortices stretching and bending around *KH*4 vortices. Vertical Kelvin–Helmholtz vortices *KH*3 (near the bottom) rise to the top and bend around Kelvin–Helmholtz vortex *KH*1. This array of vortices is identified as *V*1 in Figure 11(c).

At $\tilde{t} = 6.25$ (Figure 11(d)) vortices *V*1 and *KH*3 strengthen while the other Kelvin–Helmholtz vortices twist, bend and interact with each other, resulting in several clusters of smaller scale vortices. At the body of the current a secondary flow starts to move inward as a result of the Coriolis force in the negative radial direction. This inward flow gives origin to a set of hairpin vortices oriented toward the centre of the domain (vortices *HP*1 in Figure 11(d)). Figure 1(a) shows a closeup bottom view of these hairpins visualised by an iso-surface of $\tilde{\lambda}_{ci} = 3$. Figure 1(b) shows a stereoscopic visualisation of vortex structures in the current for case (5) at $\tilde{t} = 6.25$. The figure must be viewed with red–blue glasses. A better understanding of the vortex structure for case (5) at this time can be gained with the video supplied as supplementary material SupMatVideo8.avi.

At $\tilde{t} = 8$ and $\tilde{t} = 9$ (Figure 12(a,b)), respectively, the array of vertical vortices *KH*3 at the front and vortices *V*1 stretch in the radial direction and move in the azimuthal direction. The clusters of small scale vortices interact in a complex manner, making it difficult to distinguish individual coherent vortex structures other than the vertical vortex *VV*1.

At time $\tilde{t} = 10$ (Figure 12(c)), vertical Kelvin–Helmholtz vortices *KH*3 and *V*1 tilt and stretch in the tangential direction as a result of rotation, and hairpin vortices *HP*2 start to form at the front aligned in the azimuthal direction.

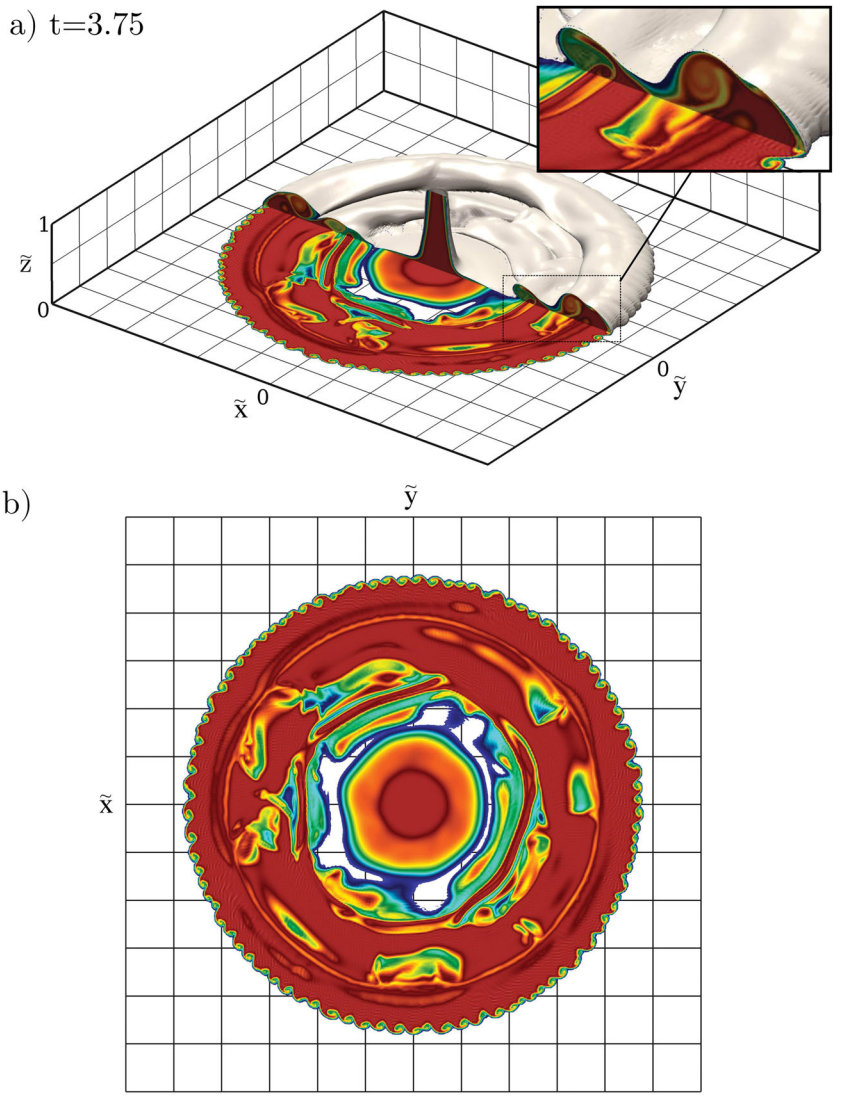

Figure 13. (a) Three-dimensional structure of the interface for case (5) visualised by a density iso-surface of $\tilde{\rho} = 0,05$ for $\tilde{t} = 3.75$. Also in this figure are depicted two slices of the density field: one for plane $\tilde{y} = 0$ (see inset figure) and another for plane $\tilde{z} = 0.05$. (b) Top view of density in plane $\tilde{z} = 0.05$ for same case and time.

After $\tilde{t} = 12.5$ (Figure 12(d)) the structures present in the flow are too weak (low values of $\tilde{\lambda}_{ci}$) to be identified.

3.3. Lobe and cleft structures at the front

The lobe and cleft structure at the front of gravity currents seen in Figures 11 and 12 is very distinctive of these flows [2,3,7,9]. In the case of 'no-slip' bottom boundary conditions, a layer of light fluid penetrates below the heavy fluid within the head resulting in an unstable stratification. Hartel et al. [45] propose that the formation of lobes and cleft originates from a gravitational instability at the unstably stratified region of the current front. Cantero et al.

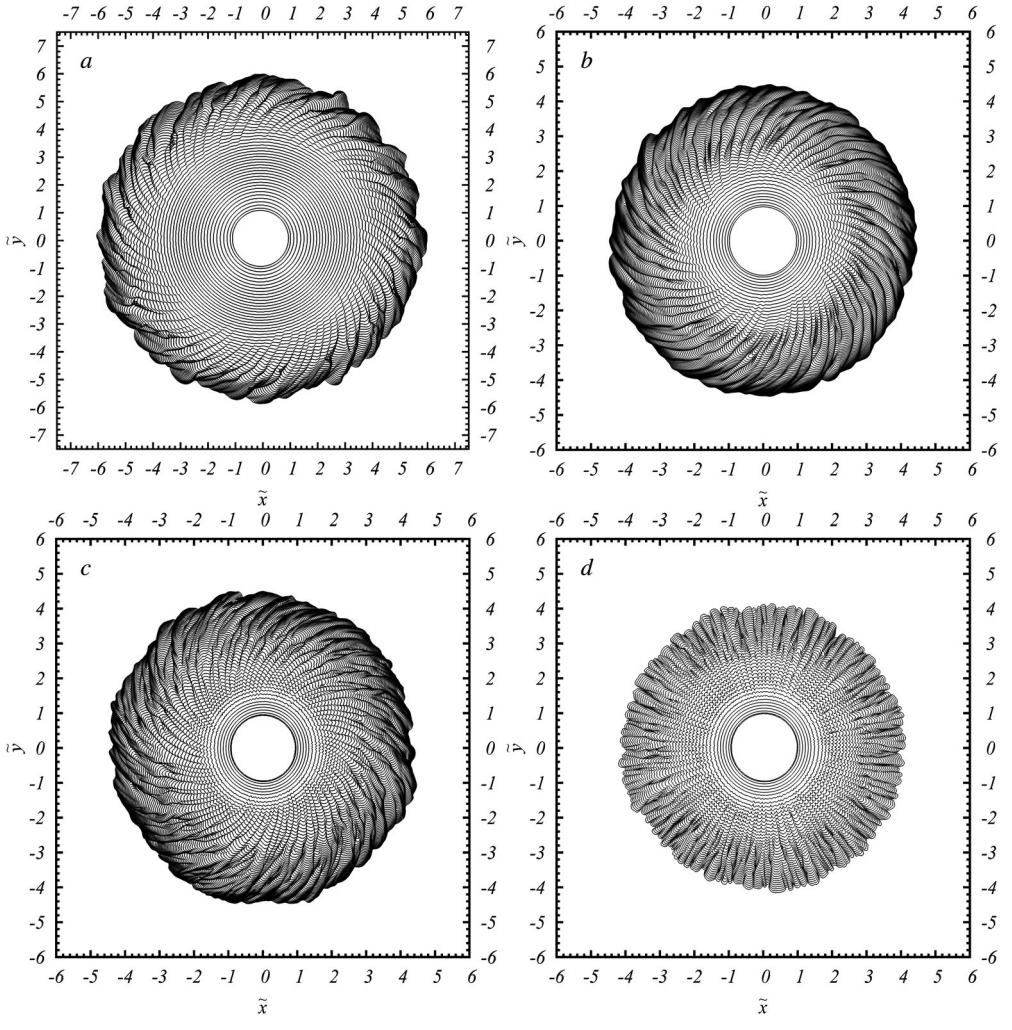

Figure 14. Composite view of the front location visualised by contours of density $\tilde{\rho} = 0.05$ in plane $\tilde{z} = 0$. The time separation between the front locations is $\Delta\tilde{t} = 0.25$. (a) Case (2): Re = 4000, Sc = 1, $\mathcal{C} = 0.15$ and 'free-slip' boundary conditions (BC) at the bottom. (b) Case (4): Re = 4000, Sc = 1, $\mathcal{C} = 0.15$ and 'no-slip' BC. (c) Case (5): Re = 8000, Sc = 1, $\mathcal{C} = 0.15$ and 'no-slip' BC. (d) Case (6): Re = 8000, Sc = 1, $\mathcal{C} = 0$ and 'no-slip' BC.

[8] present details of the lobe and cleft structure in cylindrical gravity currents with 'no-slip' bottom boundary conditions from highly resolved simulations and laboratory experiments in the absence of rotation. The existence of the lobe and cleft structure for the case of 'free-slip' bottom boundary conditions in the absence of rotation is not certain. Hartel et al. [20] report that lobe and cleft structure is not present in the case of 'free-slip' bottom boundary conditions (see also [46]).

Interestingly enough, the simulations presented in this work clearly show that, under the effect of rotation, gravity currents acquire the lobe and cleft structure even for 'free-slip' bottom boundary conditions. These features can be seen for case (2) in Figure 14(a). In this figure the front of the current is tracked by the contour of density $\tilde{\rho} = 0.05$ and plotted over

Table 2. Information on the lobe and cleft structure of the front. $\bar{r}_F$ is the mean radial position of the front, N is the number of lobes observed at the front and $\tilde{\lambda}_l$ is the mean wavelength of the lobes. The table also reports the corresponding time instances, starting from the lobe and cleft structure initiation time.

Case	$\tilde{C}$	Re	$\tilde{t}$	$\bar{r}_F$	N	$\tilde{\lambda}_l$
1	0.1	4000	9.5	5.2	82 ± 2	0.39
1	0.1	4000	10	5.4	90 ± 2	0.37
1	0.1	4000	11.25	5.8	123 ± 2	0.30
1	0.1	4000	12.5	6.3	93 ± 2	0.42
2	0.15	4000	6.25	3.6	66 ± 2	0.35
2	0.15	4000	7	4.0	73 ± 2	0.34
2	0.15	4000	7.5	4.2	72 ± 2	0.36
2	0.15	4000	10	5.1	65 ± 2	0.49
2	0.15	4000	11.25	5.4	50 ± 2	0.68
3	0.25	4000	4.5	2.8	66 ± 2	0.26
3	0.25	4000	5	3.0	65 ± 2	0.29
3	0.25	4000	7.5	3.8	49 ± 2	0.49
4	0.15	4000	3.75	2.4	71 ± 2	0.21
4	0.15	4000	5	2.8	72 ± 2	0.25
4	0.15	4000	6.25	3.1	65 ± 2	0.30
4	0.15	4000	7	3.3	63 ± 2	0.33
4	0.15	4000	7.5	3.5	62 ± 2	0.35
4	0.15	4000	10	3.9	59 ± 2	0.42
4	0.15	4000	11.25	4.1	53 ± 2	0.48
5	0.15	8000	2.5	1.9	106 ± 3	0.12
5	0.15	8000	3.75	2.4	99 ± 3	0.15
5	0.15	8000	5	2.8	79 ± 3	0.23
5	0.15	8000	6.25	3.2	81 ± 3	0.25
5	0.15	8000	7	3.4	73 ± 3	0.30
5	0.15	8000	7.5	3.6	76 ± 3	0.29
5	0.15	8000	10	4.0	57 ± 3	0.44
6	0	8000	2.5	1.9	115 ± 3	0.10
6	0	8000	3.75	2.3	117 ± 3	0.12
6	0	8000	5	2.9	129 ± 3	0.14
6	0	8000	6.25	3.3	102 ± 3	0.20
6	0	8000	7	3.5	98 ± 3	0.22
6	0	8000	7.5	3.7	98 ± 3	0.24
6	0	8000	10	4.2	102 ± 3	0.26

the $\tilde{z} = 0$ plane (top view). The front location at several times separated by $\Delta\tilde{t} = 0.25$ are superposed. Corresponding figures with the lobe and cleft structure of the advancing front for cases (4), (5) and (6) can be seen in Figure 14(b–d), respectively. For cases (2), (4) and (5) (simulations in a rotating frame of reference) the total span of time plotted covers the first oscillation of the front (until $\overline{u}_r = 0$). The formation and dynamics of the lobe and cleft structure can be seen in the videos supplied as supplementary material SupMatVideo3.avi for case (2) and SupMatVideo6.avi for case (5).

At the beginning of the simulation the front evolves in an almost axisymmetric fashion for all simulations despite the small perturbations that have been introduced in the initial condition [37]. As the flow evolves the lobe and cleft structure develops for all cases. The times for the initiation of the lobe and cleft structure are reported in Table 2. Table 2 presents the radial position of the front ($\bar{r}_F$), the number of lobes observed at the front (N) and the mean wavelength of the lobes $\tilde{\lambda}_l$ defined as $\tilde{\lambda}_l = 2\pi\bar{r}_F/N$ for several time instances. The quantification of the number of lobes at the front of the current is subject to interpretation, and N is presented with the authors' interpretation error. Table 2 clearly shows that the initiation time for the lobe and cleft structure depends on the Coriolis number, and that this

time is smaller as this number increases: $\tilde{t} \approx 9.5$ for $\tilde{C} = 0.1$, $\tilde{t} \approx 6.25$ for $\tilde{C} = 0.15$, and $\tilde{t} \approx 4.5$ for $\tilde{C} = 0.25$. The initiation of the lobe and cleft structure in the case of a 'free-slip' bottom boundary condition under the effect of rotation is directly related to the initiation of vertical Kelvin–Helmholtz vortices at the front of the current resulting from shear between the light and heavy fluids at the front (observe and compare SupMatVideo3.avi and SupMatVideo4.avi supplied as supplementary material).

The flows in cases (4), (5) and (6) with a 'no-slip' bottom boundary condition start to develop the lobe and cleft structures rather quickly as compared to case (2) with a 'free-slip' bottom boundary condition (see Table 2). Cases (2) and (4) present a direct comparison since they only differ by the bottom boundary condition. The lobe and cleft structure starts to develop at $\tilde{t} \approx 3.75$ for case (4) while for case (2) this happens at $\tilde{t} \approx 6.25$ as reported in Table 2.

Comparing case (5) and case (6) in Table 2, it is observed that fewer lobes form in the presence of rotation (see cases (5) and (6) in Table 2 at $\tilde{t} = 2.5$). For case (6) the number of lobes goes to a small period of adjustment where N increases first and then decreases. This adjustment lasts until $\tilde{t} \approx 6.25$ and then N stays approximately constant (see also [8]). On the other hand, N decreases monotonically with time for case (5). The decrease in N for case (5) indicates that more lobe merging occurs than splitting in Figure 14(c). The mean wavelength $\tilde{\lambda}_l$ of the lobes is very similar for case (5) and case (6) in the early stages of formation, but $\tilde{\lambda}_l$ increases substantially after $\tilde{t} = 3.75$ for case (5) owing mainly to lobes merger. The increases of $\tilde{\lambda}_l$ for case (6) corresponds to the increase of $\bar{r}_F$ rather than to a decrease of N. From $\tilde{t} = 7.5$ to $\tilde{t} = 10$ the mean wavelength increases by 50% for case (5) while for case (6) this increase is only 8%. This effect is clearly related to the growth of the Coriolis force in the negative radial and azimuthal directions for $\tilde{t} \approx 6$ (see Section 3.2). The deceleration of the flow in the radial direction and the azimuthal rotation induced by rotation produce an increased merging of lobes for case (5) as compared to case (6) without rotation.

Another effect of rotation on the lobe and cleft structure can be seen comparing Figures 14(c) and 14(d) for cases (5) and (6), respectively. Although the disturbances introduced in the initial condition quickly develop into the lobe and cleft structures for both cases, in a rotating frame of reference these structures move in the azimuthal direction over time generating the characteristic footprint of rotating gravity currents.

The flow pattern and turbulent structures associated with the lobe and cleft structure of the front are seen in Figure 15. Figure 15(a) shows a top view of the near-bed flow at the front of the current for case (6) at $\tilde{t} = 3.75$. The front is visualised by the density contour $\tilde{\rho} = 0.05$ at $\tilde{z} = 0.05$ (thick black line). The vector field shows the horizontal flow ($\tilde{u}_x$ and $\tilde{u}_y$ components) at $\tilde{z} = 0.05$. Also shown in this figure are the contours of vertical velocity ($\tilde{u}_z$) at $\tilde{z} = 0.05$ (yellow: positive and blue: negative) and an iso-surface of $\tilde{\lambda}_{ci} = 2$ identifying hairpin vortices. Figure 15(b) is a front view of the current front for cases (6) for $\tilde{t} = 3.75$ at the location of cut AB in Figure 15(a) showing streamlines of the vertical flow field ($\tilde{u}_x$ and $\tilde{u}_z$ components). Also shown in Figure 15(b) are the contours of vertical velocity ($\tilde{u}_z$, yellow: positive and blue: negative). Corresponding figures for case (5) are shown in Figure 15(c,d).

The horizontal flow in the clefts for case (6) is slower than in the lobes and it deviates in the azimuthal direction from the centre of the lobes to the clefts (Figure 15(a)). This flow forms a pattern of near-bottom low-speed streaks at the front. Cantero et al. [6] report these

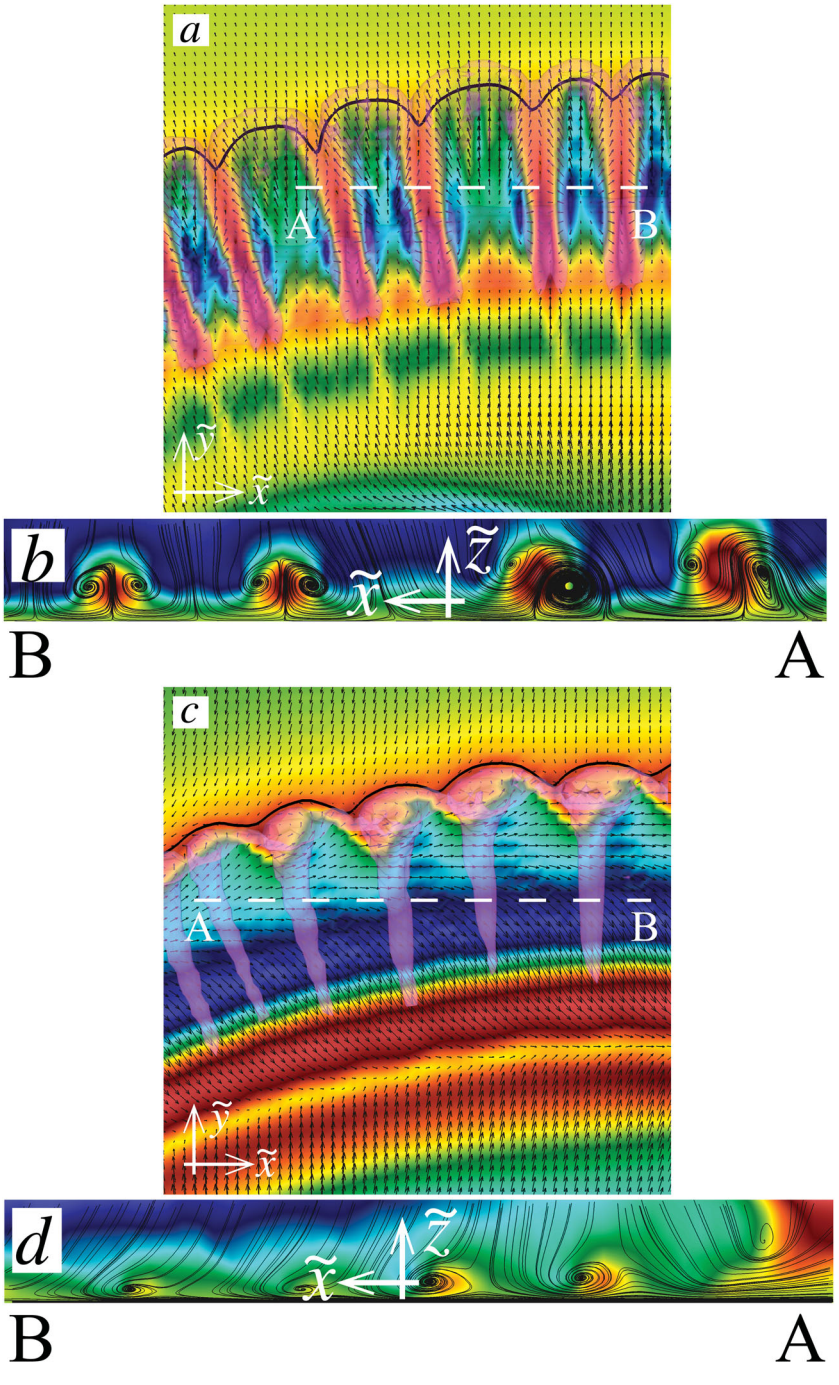

Figure 15. Visualisation of the current front near-bed flow at $\tilde{t} = 3.75$ for (a, b) the non-rotating case (6) and (c, d) the rotating case (5). (a) and (c): top view of the front visualised by the iso-contour $\tilde{\rho} = 0.05$ at $\tilde{z} = 0.05$ (thick black line). The vector field shows the horizontal flow ($\tilde{u}_x$ and $\tilde{u}_y$) at $\tilde{z} = 0.05$. Colour contours show vertical velocity $\tilde{u}_z$ at $\tilde{z} = 0.05$ (yellow: positive and blue: negative) and an iso-surface of $\tilde{\lambda}_{ci} = 2$. The white dashed lines indicate the location of the vertical slices AB displayed in frames (b) and (d). (b) and (d): side view of the current in the vertical planes AB for cases (6) and (5). Solid lines are streamlines in the vertical plane. Colour contours show vertical velocity ($\tilde{u}_z$, yellow: positive and blue: negative). In (c) and (d), the velocity field is shown in the rotating frame of reference.

front near-bottom low-speed streaks for planar currents. The low speed streaks result from the uplifting of low momentum fluid generated by the circulation cells seen in Figure 15(b). This flow pattern has been postulated by Allen [2] and described in some detail by Cantero et al. [8] from highly resolved simulations of cylindrical gravity currents in the absence of rotation.

The iso-surface of $\tilde{\lambda}_{ci}$ in Figure 15(a) for case (6) shows hairpin vortices forming at every lobe. The length scale of these hairpins is the lobe size. Cantero et al. [8] reported quasi-streamwise bottom vortices at the cleft locations, and the present simulations clearly show that these vortices were in fact the legs of the hairpin vortices that form at the front. Allen [2] postulated the existence of pairs of counter-rotating vortices at the lobes, and Figure 15(a) shows that the flow pattern is a consequence of a complete hairpin vortex at every lobe.

It is interesting to note that the flow pattern shown in Figure 15(a) for the vertical velocity $\tilde{u}_z$ indicates that the legs of the hairpin vortices rotate so that the fluid between them is pumped downward. This is opposite to the sense of rotation of hairpin vortices seen in boundary layers [47]. This is clearly seen in Figure 16(a,b) which shows details of the flow field at the front of the current in relation to the local hairpin vortices for case (6). Figure 16(a) is a composed figure showing hairpin vortices visualised by a $\tilde{\lambda}_{ci} = 2$ iso-surface and the current front visualised by a $\tilde{\rho} = 0.05$ iso-surface. The vertical plane shows $\tilde{\lambda}_{ci}$ contours and vector velocity field of the flow. The front velocity has been subtracted from the velocity flow field. The inset in Figure 16(a) shows that the location of the vertical plane is at the centre of a hairpin vortex. Figure 16(b) shows a detail of the velocity vector field of the flow at the hairpin head corresponding to the area marked with dashed lines in Figure 16(a).

Under the effects of rotation, the formation and evolution of vortex structures at the front is quite different. The internal flow rotation rolls-up the density interface at the front forming vertical Kelvin–Helmholtz vortices identified as *KH*3 in Figure 11(b). Figure 15(c) for case (5) shows a top view of the near-bed flow at the front of the current for case (5) at $\tilde{t} = 3.75$. Figure 15(d) is a front view of the current front for cases (5) for $\tilde{t} = 3.75$ at the location of cut AB in Figure 15(c) showing streamlines of the vertical flow field ($\tilde{u}_x$ and $\tilde{u}_z$ components) for case (5) at $\tilde{t} = 3.75$. The rigid body rotation velocity has been subtracted from the velocity field. The effect of rotation on the turbulent structures at the front can be seen by comparing Figures 15(a) and 15(b) with Figures 15(c) and 15(d). Figure 15(c) shows that the horizontal flow field at the lobes is not directed in the azimuthal direction towards the clefts as in case (6) (see Figure 15(a)). Instead, an anticlockwise circulation at the lobes is produced consistent with the vertical Kelvin–Helmholtz vortices. Figure 15(c) also shows that the vertical flow is upward in the lobes and clefts for $\tilde{z} = 0.05$ where the vertical Kelvin–Helmholtz vortices are, as opposed to case (6) for which the flow is upward at the cleft locations only (see Figure 15(a)). Figure 15(d) shows the flow pattern consistent with the horizontal streamwise portion of the Kelvin–Helmholtz vortices *KH*3 (Figure 11(b)), which is quite different from the flow pattern seen in Figure 15(b).

The comparison of the vortical structures at the front of non-rotating/rotating gravity currents with/without bottom friction is depicted in Figure 16. While hairpin vortices are clearly visible in the non-rotating current (Figure 16(a,b)), they are absent from the rotating cases. In rotating cases, however, vertical Kelvin–Helmholtz vortices can be observed (Figure 16(c,d)). When a free-slip boundary condition is used (Figure 16(c)) these vortices are almost perpendicular to the bottom, while in the case of no-slip boundary condition,

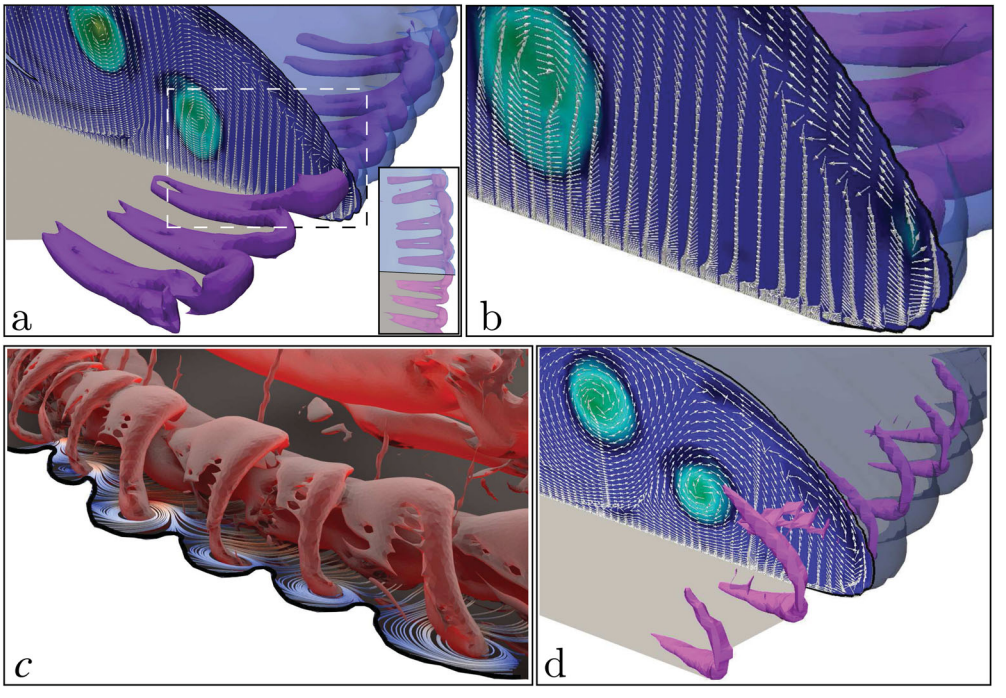

Figure 16. Visualisation of the vortical structures for (a, b) the non-rotating case (6), (c) the rotating F.S. case (2) and (d) the rotating N.S. case (5). (a) and (d): composed figure showing (a) hairpin vortices visualised by a $\lambda_{ci} = 2$ iso-surface for case (6) and (d) vertical Kelvin–Helmholtz vortices visualised by a $\lambda_{ci} = 4$ iso-surface for case (5). The current front is visualised by a $\tilde{\rho} = 0.05$ iso-surface. The vertical plane shows λ_{ci} contours and vector velocity field of the flow. The front velocity has been subtracted from the velocity flow field for case (6) and the rigid body rotation has been subtracted from the velocity flow field for case (5). The inset in frame (a) shows the location of the vertical plane, which is at the centre of a hairpin vortex for case (5) making it possible to clearly identify the sense of rotation of the head of the hairpin vortex. In frame (c) the vertical plane is located at the middle point between vertical Kelvin–Helmholtz vortices. (b) Zoom of the flow in the area marked with dashed lines in frame (a). (c) Vertical Kelvin–Helmholtz vortices visualised by a $\lambda_{ci} = 3$ iso-surface for case (2).

the vertical Kelvin–Helmholtz vortices are connected to some near-bed quasi-streamwise vortices.

4. Summary and conclusions

This work presents highly resolved simulations of cylindrical gravity currents with rotational effects, focusing on flows with small Coriolis numbers (equivalently large Rossby numbers) for which the gravity current develops its intrinsic characteristics before being affected by rotation. In this sense the present work complements the vast body of investigations on the dynamics of rotating stratified fluids, developed mainly in the area of geophysical flows, which assumed large Coriolis numbers (equivalently small Rossby numbers).

Highly resolved simulations have been performed for three different Coriolis numbers $\tilde{\mathcal{C}} = 0.1$, 0.15 and 0.25, and two different Reynolds numbers $\mathrm{Re} = 4000$ and 8000 with resolutions of up to 165-million grid points.

One of the most distinct effects of rotation is the inhibition of the flow to continuously spread (geostrophic adjustment). When the heavy fluid is released and starts to move in the positive radial direction, a Coriolis force in the negative tangential direction develops. The tangential Coriolis force induces flow in this direction, producing a Coriolis force component in the negative radial direction, which eventually interacts with the buoyancy force slowing the front down. Eventually, the radial momentum balance is mainly between Coriolis and buoyancy forces. Under these conditions the currents acquire a lens shape. The lens shape is reached through a transient in which the front of the current oscillates back and forth several times as a consequence of the transient imbalance of the buoyancy and Coriolis forces (inertial oscillations).

The main flow characteristics obtained in the present simulations are in reasonably good agreement with experimental observations [24] and theoretical models, namely box-model [29] and shallow-water equations [28]. In particular, the mean oscillation frequency $\overline{\omega}_p$ is found to satisfy the experimental linear relation $\overline{\omega}_p \approx 2\tilde{\mathcal{C}}$, and the maximum distance of propagation of the front $\bar{r}_{\max}$ scales as $1/\tilde{\mathcal{C}}^{1/2}$. Note, however, that $\bar{r}_{\max}$ found in the simulations using no-slip boundary conditions (Figure 4(b)) is somewhat smaller than the experimental results of [24]. This may be an effect of the Reynolds number which is about 50 times lower in the simulations than in the experiments ($\mathrm{Re} = 2.09 \times 10^5$ for R11 and $\mathrm{Re} = 2.93 \times 10^5$ for R6 of [24], while $\mathrm{Re} = 4 - 8 \times 10^3$ in the present numerical simulations).

The bottom boundary condition has an influence on the flow development. In the case of 'no-slip' bottom boundary conditions the values of the Coriolis force are reduced close to the bottom and cannot fully balance the buoyancy force. As a consequence, a steady state lens shape is never reached. At this stage, however, the front advances at a velocity of only $\overline{u}_F \approx 10^{-4}$. Another effect of the 'no-slip' bottom boundary condition is that the maximum radius of the successive outward fronts are not smaller than in the previous oscillations, as opposed to the cases with 'free-slip' bottom boundary condition. This behaviour was also reported by Hallworth et al. [24] from laboratory observations.

The high resolution of the simulations allows for the identification of several turbulent structures in the flow. A detailed description of the structures' evolution is presented. In the absence of rotation, the simulations show the formation of large hairpin vortices at the front. These hairpin vortices' locations coincide with the lobes' locations and they span the complete width of the lobes. Interestingly enough, the flow pattern at the front shows that the legs of the hairpin vortices rotate in the opposite sense as compared to hairpins found in boundary layers, inducing upward flow at the cleft locations and downward flow at the lobes locations.

Under the influence of rotation, the flow pattern completely changes at the front of the current displaying vertical Kelvin–Helmholtz vortices in place of the hairpin vortices seen in the absence of rotation.

Finally, the manuscript also reports on the lobe and cleft structure of the front. Although the existence of these structures for the case of *"free-slip"* bottom boundary conditions is not certain, the simulations presented in this work clearly show that gravity currents acquire the lobe and cleft structure at the front under the effect of rotation. The initiation of the lobe and cleft structure under these circumstances is directly related to the initiation of vertical Kelvin-Helmholtz vortices at the front of the current. These vortices develop more rapidly in the case of 'no-slip' bottom boundary conditions, even before rotational effects become

dominant. The net effect of rotation on the lobe and cleft structure is an augmentation of lobe merging produced by the deceleration of the flow (induced by the Coriolis force in the negative radial direction) and the azimuthal rotation (induced by the Coriolis force in the azimuthal direction).

It should be mentioned that in the present simulations, the value of the Schmidt number is set to unity. However, contrary to non-rotating gravity currents, the *thickness* of the front is not sharp anymore (see e.g. Figure 6) but rather spreads up to several initial radii. The processes involved in such a spreading may be, among others, mass diffusion enhanced by convective mixing. One thus may wonder if Schmidt effects may play a role in the present rotating configuration. Such an investigation is beyond the scope of the present paper and is left for future work.

Acknowledgements

The work presented in this manuscript is part of the M.S. thesis of Jorge Salinas at Instituto Balseiro finished and published in 2014, with a scholarship by the National Commission of Atomic Energy of Argentina (CNEA). Mariano Cantero and Enzo Dari acknowledge the financial support of ANPCyT with PICT-2575, CNEA and CONICET. Mariano Cantero and Thomas Bonometti acknowledges the financial support of INPT with SMI 2015. Some of the computational time was provided by the Scientific Groupment CALMIP (project P1525), the support of which is greatly appreciated.

Disclosure statement

No potential conflict of interest was reported by the authors.

Funding

ANPCyT (Fondo para la Investigación Científica y Tecnológica) [grant number PICT-2575]; INPT [grant number SMI 2015]; Scientific Groupment CALMIP [project number P1525].

References

[1] García M. Turbidity currents. In: Brekhovskikh L, Turekian K, Emery K, et al., editors. Encyclopedia of earth system science. Vol. 4. New York (NY): Academic Press, Inc.; 1992. p. 399–408.
[2] Allen J. Principles of physical sedimentology. London, UK: George Allen and Unwin Ltd.; 1985. 272 pages.
[3] Simpson JE. Gravity currents in the environment and the laboratory. Cambridge (UK): Cambridge University Press; 1997.
[4] Griffiths SW. Gravity currents in rotating systems. Ann Rev Fluid Mech. 1986;18:59–89.
[5] Hopfinger E, van Heijst G. Vortices in rotating fluids. Ann Rev Fluid Mech. 1993;25:241–289.
[6] Cantero M, Balachandar S, García M, et al. Turbulent structures in planar gravity currents and their influence of the flow dynamics. J Geophys Res Oceans. 2008;113:C08018.
[7] Simpson J. Effects of the lower boundary on the head of a gravity current. J Fluid Mech. 1972;53(4):759–768.
[8] Cantero M, Balachandar S, García M. Highly resolved simulations of cylindrical density currents. J Fluid Mech. 2007;590:437–469.
[9] Allen J. Mixing at turbidity current heads, and its geological implications. J Sedimentary Petrology. 1971;41(1):97–113.
[10] Hoult D. Oil spreading in the sea. Ann Rev Fluid Mech. 1972;4:341–368.

[11] Fannelop T, Waldman G. The dynamics of oil slicks – or 'creeping crude'. AIAA J. 1971;41:1–10.
[12] Huppert H, Simpson J. The slumping of gravity currents. J Fluid Mech. 1980;99:785–799.
[13] Marino B, Thomas L, Linden P. The front condition for gravity currents. J Fluid Mech. 2005;536:49–78.
[14] Patterson M, Simpson J, Dalziel S, et al. Vortical motion in the head of an axisymmetric gravity current. Phys Fluids. 2006;18(4):046601-1/7.
[15] Alahyari A, Longmire E. Development and structure of a gravity current head. Exp Fluids. 1996;20:410–416.
[16] Simpson J, Britter R. The dynamics of the head of a gravity current advancing over a horizontal surface. J Fluid Mech. 1979;94:477–495.
[17] García M, Parsons J. Mixing at the front of gravity currents. Dyn Atmos Oceans. 1996;24:197–205.
[18] Parsons J, García M. Similarity of gravity current fronts. Phys Fluids. 1998;10(12):3209–3213.
[19] Thomas L, Dalziel S, Marino B. The structure of the head of an inertial gravity current determined by particle-tracking velocimetry. Exp fluids. 2003;34:708–716.
[20] Härtel C, Meiburg E, Necker F. Analysis and direct numerical simulation of the flow at a gravity-current head. Part 1. Flow topology and front speed for slip and no-slip boundaries. J Fluid Mech. 2000;418:189–212.
[21] Blanchette F, Strauss M, Meiburg E, et al. High-resolution numerical simulations of resuspending gravity currents: condition for self-sustainment. J Geophys Res. 2005;110:c12022.
[22] Birman V, Martin J, Meiburg E. The non-Boussinesq lock-exchange problem. Part 2. High resolution simulations. J Fluid Mech. 2005;537:125–144.
[23] Cantero M, Lee JR, Balachandar S, et al. On the front velocity of gravity currents. J Fluid Mech. 2007;586:1–39.
[24] Hallworth M, Huppert H, Ungarish M. Axisymmetric gravity currents in a rotating system: experimental and numerical investigations. J Fluid Mech. 2001;447:1–29.
[25] Stegner A, Bouruet-Aubertot P, Pichon T. Nonlinear adjustment of density fronts. Part 1. The Rossby scenario and the experimental reality. J Fluid Mech. 2004;502:335–360.
[26] Stegner A. Experimental reality of geostrophic adjustment. In: Zeitlin V, editor. Nonlinear dynamics of rotating shallow water: methods and advances. Amsterdam: Elsevier; 2007.
[27] Kuo A, Polvani L. Nonlinear geostrophic adjustment, cyclone/anticyclone asymmetry, and potential vorticity rearrangement. Phys Fluids. 2000;12(5):1087–1100.
[28] Ungarish M. An introduction to gravity currents and intrusions. Boca Raton, FL: CRC Press; 2009.
[29] Ungarish M, Huppert H. The effects of rotation on axisymmetric gravity currents. J Fluid Mech. 1998;362:17–51.
[30] Ungarish M, Huppert H. Simple models of coriolis-influenced axisymmetric particle-driven gravity currents. Int J Multiphase Flow. 1999;25:715–737.
[31] Salinas JS. Modeling and simulation of gravity currents with rotational effects [M.S. thesis]. Bariloche, Río Negro, Argentina: Instituto Balseiro, CNEA-UNC; 2014. Spanish.
[32] Blumen W. Geostrophic adjustment. Rev Geophys Space Phys. 1972;10:485–528.
[33] Griffiths R, Linden P. The stability of vortices in a rotating, stratified fluid. J Fluid Mech. 1981;105:283–316.
[34] Verzicco R, Lalli F, Campana E. Dynamics of baroclinic vortices in a rotating, stratified fluid: a numerical study. Phys Fluids. 1997;9:419–432.
[35] Canuto C, Hussaini M, Quarteroni A, et al. Spectral methods in fluid dynamics. New York (NY): Springer-Verlag; 1988. 557 pages.
[36] Durran D. Numerical methods for wave equations in geophysical fluid dynamics. Seattle: Springer; 1999.
[37] Cantero M, Balachandar S, García M, et al. Direct numerical simulations of planar and cyindrical density currents. J Appl Mech. 2006;73:923–930.

[38] Salinas J, Cantero M, Dari E. Simulación directa de turbulencia en corrientes de gravedad con effectos de coriolis [Direct numerical simulations of gravity currents with Coriolis effects]. Revista Iberoamericana del Agua. 2014;1:26–37.
[39] Bonometti T, Balachandar S. Effect of the schmidt number on the structure and propagation of density currents. Theoret Comput Fluid Dyn. 2008;22:341–361.
[40] Shin J, Dalziel S, Linden P. Gravity currents produced by lock exchange. J Fluid Mech. 2004;521:1–34.
[41] Wirth A. On the basic structure of oceanic gravity currents. Ocean Dyn. 2009;59:551–563.
[42] Necker F, Härtel C, Kleiser L, et al. High-resolution simulations of particle-driven gravity currents. Int J Multiphase Flow. 2002;28:279–300.
[43] Zhou J, Adrian R, Balachandar S, et al. Mechanics for generating coherent packets of hairpin vortices in channel flow. J Fluid Mech. 1999;387:353–396.
[44] Chakraborty P, Balachandar S, Adrian R. On the relationships between local vortex identification schemes. J Fluid Mech. 2005;535:189–214.
[45] Härtel C, Carlsson F, Thunblom M. Analysis and direct numerical simulation of the flow at a gravity-current head. Part 2. The lobe-and-cleft instability. J Fluid Mech. 2000;418:213–229.
[46] Britter R, Simpson J. Experiments on the dynamics of a gravity current head. J Fluid Mech. 1978;88:223–240.
[47] Adrian R. Hairpin vortex organization in wall turbulence. Phys Fluids. 2007;041301:1–16.